



Article

Prediction Model of Alcohol Intoxication from Facial Temperature Dynamics Based on K-Means Clustering Driven by Evolutionary Computing

Jan Kubicek ^{1,*}, Dominik Vilimek ¹, Alice Krestanova ¹, Marek Penhaker ¹ , Eva Kotalova ¹, Bastien Faure-Brac ², Clément Noel ², Radomir Scurek ³, Martin Augustynek ¹, Martin Cerny ¹  and Tomas Kantor ³

¹ Department of Cybernetic and Biomedical Engineering, VŠB—Technical University of Ostrava, 17, listopadu 15, 708 33 Ostrava, Poruba, Czech Republic

² Pôle MSTIC; UGA—Polytech Grenoble, IESE, 14 Place du Conseil National de la Résistance, 38400 St-Martin-d'Hères, France

³ Department of Security Services, VŠB—Technical University of Ostrava, Lumírova 13/630, 700 30 Ostrava, Výškovice, Czech Republic

* Correspondence: jan.kubicek@vsb.cz

Received: 28 May 2019; Accepted: 24 July 2019; Published: 3 August 2019



Abstract: Alcohol intoxication is a significant phenomenon, affecting many social areas, including work procedures or car driving. Alcohol causes certain side effects including changing the facial thermal distribution, which may enable the contactless identification and classification of alcohol-intoxicated people. We adopted a multiregional segmentation procedure to identify and classify symmetrical facial features, which reliably reflects the facial-temperature variations while subjects are drinking alcohol. Such a model can objectively track alcohol intoxication in the form of a facial temperature map. In our paper, we propose the segmentation model based on the clustering algorithm, which is driven by the modified version of the Artificial Bee Colony (ABC) evolutionary optimization with the goal of facial temperature features extraction from the IR (infrared radiation) images. This model allows for a definition of symmetric clusters, identifying facial temperature structures corresponding with intoxication. The ABC algorithm serves as an optimization process for an optimal cluster's distribution to the clustering method the best approximate individual areas linked with gradual alcohol intoxication. In our analysis, we analyzed a set of twenty volunteers, who had IR images taken to reflect the process of alcohol intoxication. The proposed method was represented by multiregional segmentation, allowing for classification of the individual spatial temperature areas into segmentation classes. The proposed method, besides single IR image modelling, allows for dynamical tracking of the alcohol-temperature features within a process of intoxication, from the sober state up to the maximum observed intoxication level.

Keywords: image segmentation; IR image; evolutionary optimization; ABC; alcohol intoxication; features tracking

1. Introduction

Alcohol, in particular ethanol, is one of the most significantly consumed drugs worldwide. As far as we know, alcohol significantly contributes to the total number of hospital admissions and deaths, mainly including those due to car accidents and overdose [1,2]. The molecule which is responsible for alcohol intoxication is the ethanol (C₂H₆O). Present in all alcoholic beverages, ethanol reaches the blood vessel system through normal digestion. Recognized as a toxin, ethanol is destroyed by the body; mainly in the liver, as it filters blood [1–4].

When the input of ethanol in the body is superior to the liver's absorption capacity, for example, when we drink, ethanol stacks in the bloodstream, and begins to have all sorts of effects. As a small molecule, ethanol will make its way through most of our organs, including the brain, which induces the most visible part of intoxication. Immediately after reaching the blood vessels system, ethanol can be presented in the expired air. It is estimated that the air concentration is proportional to ($\times 2100$ at 294°), making it a very good estimator, in theory. As accessing the breath of a person is relatively easy, this technique has been the most widely used to estimate BAC (blood alcohol content), through devices called breathalyzers [5–8].

Since alcohol affects nearly all social areas, there is an urgent need to develop methods which can precisely estimate the alcohol content in the human body and predict a tissue damage caused by alcohol intoxication (BAC). Generally, each active substance may be effective only when reaching a place it can affect [9,10]. It must resorb in the human body. The acute intoxication can be classified into four stages (Table 1) [11,12].

One of the most popular methods for alcohol measurement is breath analysis. We recognize three types: electrochemical, based on the oxidation of ethanol into acetic acid and water, producing a measurable anode–cathode current; semiconductor-based, using a material whose resistance varies with the amount of ethanol on its surface; and spectrophotometers operating in the near infrared spectrum (NIR), which can detail measure the exhaled air's composition. The latter is extremely accurate and is used by police [5,6,12].

One of the major limitations of the conventional methods is that they require the intervention and agreement of the tested person. Secondly, these methods allow for only the on-the-spot measurement, which means current alcohol content. In our study, we take advantage the fact that gradual alcohol intoxication is accompanied by features allowing for an estimate of gradual intoxication. One of such features is facial thermal distribution, which shows differences in the spatial temperature map whilst drinking, in comparison with the sober state [13–16]. A mathematical model which is able to automatically extract the facial areas which the best reflect the level of alcohol intoxication would significantly contribute to the study of the dynamical alcohol effect on the human body, and at the same time such method would provide a contactless method for the measurement of alcohol intoxication. Nevertheless, we should consider its limitations: it identifies only the remaining alcohol, and various people may have different alcohol inclination, which may result in different thermal effects [17–19].

Based on the experimental observations, we indicate that the nose and forehead well reflect the dynamical progress of the temperature distribution whilst drinking alcohol. The nose area is mostly represented by colder intensity spectrum, and it is expected this intensity spectrum is reduced with increased alcohol intoxication. Contrarily, the forehead is represented by pixel values indicating a higher temperature which is expanded with intoxication. These alcohol-features may serve as good predictors of a dynamical progress of alcohol intoxication.

We suppose that the temperature distribution may be observable from the IR image records, which are intended for mapping of thermal distribution. In this sense, the clustering may be able to identify finite groups of pixels representing different facial thermal features. Such an approach would allow for classification of the IR facial images into a finite number of the segmentation classes. This model allows for extraction of the dynamical features serving as predictors for alcohol intoxication. In our study, we propose the multiregional segmentation model which is based on a hybrid approach, including K-means clustering and a modified ABC evolutionary algorithm. The ABC algorithm is focused for the optimization of cluster definition with the goal to define the most homogenous symmetrical clusters as possible, which reflect facial temperature maps during alcohol intoxication.

On the other hand, we are aware of certain limitations of facial temperature modeling. The experimental measurements should be done via standardized conditions, tested persons should not use any medicaments would influence the thermoregulation, and alcohol inclination can also play an important role. There are other limitations which may influence facial temperature distribution such

as wearing glasses, make up, adipose tissues, age, gender, anthropometry, circadian rhythms, hair density, skin emissivity, metabolic rate, and skin blood-flow [20–22].

In our research, we take advantage the fact that individual facial regions reflect alcohol intoxication in different ways. Furthermore, the temperature effect undergoes evolution within the time of intoxication. This dynamic effect can be automatically identified via multiregional segmentation which can identify temperature clusters into regions. Features of these regions consequently allow for the dynamical tracking of alcohol intoxication. We proposed a K-means algorithm which is driven by evolutionary optimization to build a prediction model which can identify facial temperature areas with dynamical features whilst drinking.

We did experiments with alcohol intoxication on twenty volunteers. We studied the effect of alcohol intoxication in the thermal area. We captured sober state IR images through the gradual intoxication of the subjects to study the effects of alcohol. Besides the IR images, we also recorded further information related to intoxication, e.g., the alcohol breath content or medicaments which may influence the temperature distribution within intoxication. Thermal area, in comparison with the visible spectrum, is capable of identifying facial-temperature distribution. Based on these facts, we tracked the temperature spectrum in the nose and forehead area, where these areas reflect the temperature dynamic whilst drinking.

Organization of the paper is as follows. In Section 2 we describe the recent method for alcohol intoxication. We are primarily focused on the methods, which are applied on IR images to investigate facial features whilst drinking alcohol. As a part of the review, we also refer to the IR datasets description, which are crucial for estimating alcohol intoxication from the IR images. Section 3 is dedicated to the procedure of facial IR measurement and data acquisition. Section 4 deals with the proposal of the model for estimating alcohol intoxication from IR images. Firstly, we describe the IR image preprocessing, which is aimed at improving the facial features used for the IR image segmentation. Consequently, we describe and analyze the proposed segmentation model for alcohol intoxication analysis. In Section 5, we state the results, showing alcohol intoxication analysis from the IR images, as well as correlation analysis with the alcohol breath results within intoxication. Section 6 brings the quantitative comparison of the proposed method against selected state-of-the-art methods for the application of deterministic image noise. Section 7 summarize the results and issues of the research of alcohol intoxication dynamic and points out on the limitations of image segmentation for alcohol intoxication analysis.

Table 1. Classification of the acute alcohol intoxication.

Level of Intoxication		Level of Alcohol in Blood	Features
1. Stage	Euphoria	<1%	Excitation, worsening of concentration
2. Stage	Hypnotic	1–2%	Disturbance of balance and movement coordination
3. Stage	Narcotic	2–3%	Disturbance of consciousness
4. Stage	Asphyxia	>3%	Deep coma, hypothermia

2. Related Work

Identification and tracking of alcohol intoxication's features, which are linked with real intoxication, represent a relatively new and challenging area. In our work, we investigate alcohol intoxication depending on spatial thermal distribution expressing dynamical progress exhibited whilst drinking alcohol. In comparison with the visible spectrum, IR imaging brings the opportunity to identify facial temperature distribution which is linked with the real alcohol intoxication. Thus, by using the IR imaging it is possible to track the facial-temperature features, related with intoxication. Most of the reported papers are focused on the classification: sober/drunken person from the IR images, but do not study the dynamical progress of intoxication.

In [13], Zhihua et al. adopted a combination of the wavelet transformation and discrete cosine transformation with support vector machines to identify drunken people. In [14], Koukiou et al.

proposed a concept of neural networks, which is used for alcohol intoxication classification. The authors are primarily focused on classification of the facial area. In [17], Koukiou et al. focus on analysis of the recognizable space between sober and drunken people. This analysis is done based on discriminant analysis. As a part of this analysis, the authors described tracking temperature distribution among individual face areas with the goal to recognize the most significant facial areas of drunken people. In [18], Koukiou et al. focused on facial blood vessels as one of the possible intoxication predictors of alcohol-intoxicated people analyzed based on anisotropic diffusion in combination with Top-Hat transformation. In [19], Koukiou et al. analyzed the distribution of the eye area with the main goal of the iris and sclera temperature identification to recognize drunken people. In [23], Koukiou et al. attempted to recognize drunkenness based on the application of the local difference patterns on the forehead with the goal of the extraction of significant alcohol features.

The current research shows that infrared (IR) spectrum detects specific facial features for face recognition, which cannot be acquired from the visible spectrum, [24–28]. The main idea is to track face recognition depending on physiological conditions, which are related to facial blood vessel distribution [29]. Another important part of the study of alcohol intoxication deals with analysis of the psychological properties for person identification and face recognition. Such systems have potential to be used on biometric systems [30,31]. Nevertheless, it is important to note that these studies have not been focused on alcohol-intoxicated people [32].

An important part of the research in the facial feature's extraction is the used dataset. Generally, data can be acquired via different ambient conditions, which may influence facial temperature distribution. Another important issue is particular IR camera, which may affect the facial IR images. Another issue is also used kind of the alcohol. Various people may have different inclinations to different alcohols, and this should be considered in the analysis. In [13], the camera used was the ThermoVision A40, also manufactured by FLIR Systems operating in the 8 μm –14 μm range. The data was composed as follows: 200 images of one drunken person, 200 images of the same drunk person at a different time, and 10 images of 40 sober persons, resulting in a total of 800 images evenly distributed between drunk and sober individuals. These images were then normalized in scale and positioned into 60 \times 80 px images. The environment was air-conditioned, and the temperature was kept between 24.3 $^{\circ}\text{C}$ and 25.3 $^{\circ}\text{C}$. In [17,18], authors worked with a set of the images taken from 20 individuals (12 males and 8 females), taken by the Thermal Vision Micron/A10 infrared camera manufactured by FLIR Systems Inc. This camera operated in wavelengths from 7.5 μm to 13 μm . Each person drank a 330 mL glass of beer, four times, spaced by 20 min intervals. One acquisition was made before every drink and one 20 min after the last beer. Each acquisition is composed of 50 frames, resulting in 250 frames for each person in total. Room temperature was kept constant, as well as the temperature of the beverages. The subjects were calm, rested, and in normal psychological conditions. In [14,19], beer was replaced by 120 mL glasses of red wine (13% vol.), of which 41 (31 males and 10 females) participants drank four in a one-hour time period, and acquisition occurred only at the beginning (sober), and 30 min after the last glass. The rest remained unchanged. Again, the subjects were calm, rested, and in normal psychological conditions. In all those studies, the thermograms were grayscale encoded, meaning that their values had only one dimension.

3. Facial IR Image Records and Measurement

For our analysis, we performed IR measurements, including twenty volunteers. Within the experiment, we captured six images for each tested person to track the dynamical progress of alcohol intoxication, where the first IR image corresponds with the sober state, and the others represent individual alcohol intoxication (Figure 1). The measurement procedure was done in the Faculty of Safety Engineering, in the Technical University of Ostrava on 15 December 2016 and 3 May 2017. The measuring room was airconditioned. All the measurements started at 4:00 p.m., and the outside temperature was +1 $^{\circ}\text{C}$ (15 December 2016) and 13 $^{\circ}\text{C}$ (3 May 2017). All the measurements were done via standardized conditions for the IR image capturing. The IR camera was placed at a distance of two

meters from the measured person. After all the measurements were done, the data from the IR camera were exported in the mat format, which is readable in the software MATLAB, in which we develop all the algorithms of the IR image processing.

All the tested persons came in at the agreed time, and they did not consume any food, by instruction. Besides the IR measurements, we also tracked the following parameters: age, weight, height, used medicaments (due to possible influence of the thermoregulation), heart rate, current diseases, and a subjective level of alcoholism on the following scale: 1 (abstinent) to 4 (alcoholic). Extracts of these parameters are reported in Table 2. All the probands reported they were healthy, without increased human body temperature, and had not been practising any physical activity in the last 5 h. We also tracked the blood pressure by Tonometr Sencor SBP 690, and a level of the alcohol by the breath analyzer Dräger Alcotest® 7510. Tonometr Sencor SBP 690 works on the principle of oscilometric method and have a memory for 60 measurements. This device enables the measurement range: 40–199 beats/minute. Tonometr Sencor SBP 690 is distributed in the Czech Republic by Sencor brand with the place in Ricany near Prague. The breath analyzer is approved by the Czech Metrologic Institute with the mark TCM 144/08–4644 as a set gauge. Dräger Alcotest® 7510 is distributed in the Czech Republic by Dräger Safety s.r.o. with the place in Cestlice.

Table 2. Extract of physiological parameters whilst alcohol intoxication measurement.

Sex	Age	Height [m]	Weight [kg]	Medicaments	Alcohol Breath [%]	Heart Rate [bpm]
w	25	1.7500	62	contraception	[0, 0.1700, 0.4300, 0.6700, 0.9100, 0.9200]	[82, 88, 81, 76, 75, 73]
m	23	1.7800	70	XYZAL	[0, 0.1200, 0.2900, 0.4900, 0.6800, 0.8700]	[70, 70, 67, 69, 60, 59]
m	23	1.7900	85	none	[0, 0.0900, 0.2400, 0.4000, 0.5600, 0.6500]	[86, 83, 83, 81, 85, 80]
m	23	1.8200	78	none	[0, 0.1700, 0.2900, 0.4600, 0.6300, 0.7200]	[58, 52, 53, 50, 51, 49]
m	31	1.7700	65	none	[0, 0.2300, 0.5400, 0.7400, 0.9400, 0.9500]	[93, 84, 78, 75, 73, 70]
w	47	1.7200	100	none	[0, 0.1600, 0.2600, 0.4200, 0.5500, 0.5900]	[93, 87, 86, 82, 79, 77]
w	67	1.6700	95	LORISTA	[0, 0.2100, 0.4100, 0.6400, 0.8500, 0.9300]	[80, 75, 68, 63, 63, 61]
m	23	1.8200	90	none	[0, 0.0100, 0.1600, 0.3900, 0.5200, 0.6900]	[66, 63, 70, 71, 73, 77]
m	23	1.8600	87	none	[0, 0.1700, 0.3200, 0.4900, 0.5800, 0.7100]	[50, 60, 56, 61, 63, 66]
m	25	1.8800	92	none	[0, 0.1900, 0.3200, 0.4500, 0.5900, 0.7200]	[50, 61, 56, 63, 63, 69]

In order to achieve reproducible results, and avoid facial temperature influence, all the measurements were performed indoors, via the standardized conditions including: the atmospheric pressure 1002.5 hPa, indoor temperature 22 °C and humidity 55%.

All the measurements were performed with the permission of the ethical board due to possible effect of the alcohol on the human's health. All the persons signed an agreement statement to declare not using any medicaments would influence facial temperature. Before the IR measurements, all the tested persons also had signed an agreement in the Czech language that their data could be published, and they were aware of alcohol consuming. A physician was present during all the measurements. The tested persons were perceived in a calm state for 30 min to avoid the outdoor temperature's influence. After acclimatization, all the tested persons' systolic and diastolic blood pressures were measured. Consequently, breath analysis was done. During the measurement, the tested persons were given a 38% alcohol in 0.04l doses. The gradual intoxication was driven by 30 min time intervals between individual doses.

We kept a distance of 2 m of the tested person from the IR camera with an emissivity 0.96. For the IR image background, we used white stucco plaster. All the IR images were taken by a FLIR T640 camera. This camera has an image resolution 640 × 480 px and thermal sensitivity (NETD) < 0.035 °C. For the practical purpose of the measurement, we used two kinds of the detectors: FOL41 (f = 41.3 mm, 15 °C) and FOL25 (f = 24.6 mm, 25 °C). Calibration of the IR camera was done using Flat Field Correction (FFC). This method represented an offset calibration which was performed at power up, when the IR camera was changing temperature, and consequently during the process. This

calibration compensated errors during operation of the IR camera. All the acquired IR facial images contained the conversion scale, converting the temperature scale into the color spectrum.

In our analysis, we focused on certain facial features (nose and forehead), which were analyzed for alcohol intoxication. To extract these facial areas, we use the Viola–Jones object detector. It is perceived as a strong, binary classifier, which was composed from several weak detectors. During the learning stage, a cascade of these detectors was trained to gain the desired hit rate and miss rate. For object detection, the original facial image was classified into several rectangular areas, where each of them was sent to the cascade. The rectangular image went through of all the cascade stages, then it was classified as positive. In general, each weak classifier was based on a very simple visual feature. Such kinds of features are commonly referred as “Haar-like features” [33–35].

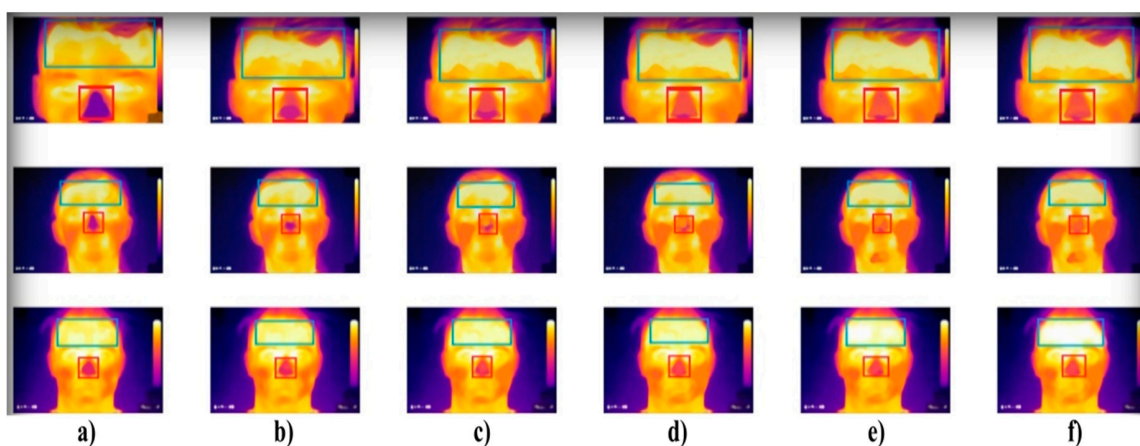


Figure 1. Extract of the IR measurement of three individuals (rows) where: (a) sober state, (b) 40 mL, (c) 80 mL, (d) 120 mL, (e) 160 mL, and (f) 200 mL of alcohol. The forehead and nose were detected by using the Viola–Jones object detection to indicate individual facial areas. The hottest area of the forehead is getting expanded, while the coldest area of the nose is getting reduced within alcohol intoxication.

4. Materials and Methods

In this section, we introduce the complex model for alcohol intoxication. The proposed model for the dynamic tracking of alcohol intoxication from the facial IR images was composed from two essential parts. Firstly, we introduce the image preprocessing with the aim to investigate the individual R, G, B layers of the IR images. This procedure leads to reflection of alcohol intoxication for individual image layers. In the consequent step, we introduce the multiregional segmentation procedure, which is aimed on separation of individual facial temperature clusters into the segmentation classes. This procedure is based on the K-means clustering, driven by the evolutionary optimization.

In this part, we introduce analysis of the IR image pre-processing. The input IR image is represented by the RGB structure containing three channels (R, G, B). We need to achieve the best observation for facial features representing alcohol intoxication. We performed a decomposition of the original RGB model into individual layers (Figure 2). Apart from identification of individual intensity sub-spectrums, this procedure also converts three dimensional RGB image into 2D space which is more convenient for the further processing. The proposed segmentation algorithm is capable of working with 2D structures, therefore, the monochromatic conversion is necessary. Furthermore, certain isolated R, G, B channels better reflect facial temperature spectrum during alcohol intoxication than the complex RGB structure. Based on these facts, the RGB decomposition is a crucial task for our study.

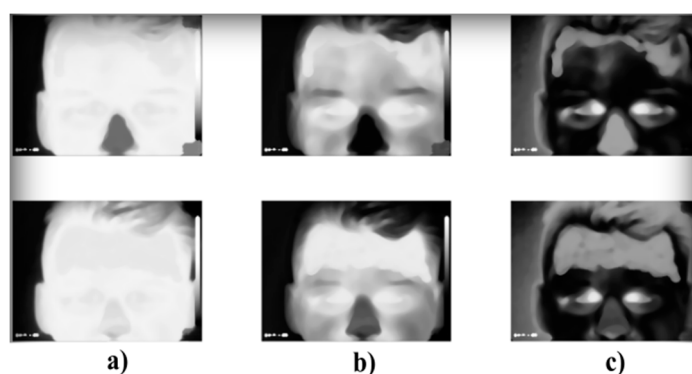


Figure 2. Comparison of the RGB decomposition for sober state (top row) and after 200 mL of 38% alcohol (down row), where: (a) R layer, (b) G layer, and (c) B layer.

Based on the RGB image decomposition, different representations of facial temperature distribution is observable on different layers. The B layer reflects the forehead's hot intensity spectrum, while the G layer reliably reflects the nose cold spectrum. Based on these features, these two models are intended for use in the modeling. Consequently, we focused on objectivization of a presence of the dynamical features in individual parts of the face, including the nose, mouth, cheeks, and forehead. Individual IR images were created by using the Viola–Jones object detector to justify which parts of the face express the most significant thermal progress whilst drinking alcohol. In this analysis, we evaluated differences between the sober state and after 100 and 200 mL of the consumed alcohol (Figure 3). The black color indicates areas with no differences, contrarily the blue color on the forehead and yellow on the nose stands for dynamical progress on the forehead and nose respectively. We performed measuring differences for the all facial regions to prove the forehead and nose are the most significant features, regarding the dynamical progress of drinking alcohol. The measurement was evaluated based on the simple differences (Diff) and Mean Squared Error (MSE). The averaged results for twenty people are reported in the Tables 3 and 4. The best results in a sense of the maximum dissimilarity are highlighted.

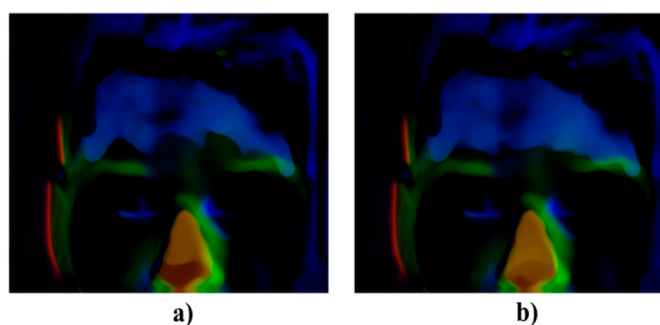


Figure 3. Showing differences of the IR image taken after (a) 100 mL of the alcohol and (b) 200 mL of alcohol against the sober state.

Table 3. Dissimilarity measurement based on the Mean Squared Error (MSE).

Alcohol State	Nose	Forehead	Cheeks	Mouth
Sober state—100 mL of alcohol	35.12	36.19	5.41	2.36
Sober state—200 mL of alcohol	44.12	49.58	6.69	5.78

Table 4. Dissimilarity measurement based on the simple average differences.

Alcohol State	Nose [%]	Forehead [%]	Cheeks [%]	Mouth [%]
Sober state—100 mL of alcohol	19.56	22.11	3.95	1.15
Sober state—200 mL of alcohol	28.15	35.87	11.15	9.42

Swarm intelligence optimization algorithms represents a rapidly emerging field, which is inspired by the collective intelligence of insect or animals organizing in groups, like in ant or bee colonies. The concept of the collective intelligence was originally introduced in [36–38] with the target to describe the self-organizing and intelligent behavior of ants. One of the most popular evolutionary algorithms is the Artificial Bee Colony algorithm (ABC) which was originally introduced in [39]. This algorithm is inspired by behavior of a honeybee swarm to solve unconstrained optimization issues [40].

In this section, we introduce the segmentation method for facial IR image features modelling. The proposed segmentation model is based on the clustering which is driven by the modified version of ABC. The ABC algorithm represents a genetic optimization process, searching for the most optimal symmetrical distribution of the clusters to achieve the most suitable approximation of the thermal areas separation, expressing significant different facial thermal features. Such a procedure is much more effective, when compared with the conventional K-means algorithm, which generates only one distribution of clusters. Such is the limitation of some clustering algorithms, it is likely the K-means may predetermine less accuracy of pixel classification because there is no unified scheme for the initial centroids' placement. We employ the modified ABC algorithm for optimal finding of the initial centroids for the facial IR images.

4.1. Segmentation Based on K-Means

We suppose that the IR image area $I(r)$, represented by the coordinates $r = \{x, y\}$, can be decomposed into a finite number of n segmentation classes forming a multiregional segmentation. In such configuration, each segmentation class specifies a finite group of the intensity spectrum expressing similar thermal features. Supposing a finite vector of the m -intensity values: $I = \{I_1, I_2, \dots, I_m\}$, which are supposed to be classified into a finite element vector of clusters: $C = \{C_1, C_2, \dots, C_{n-1}, C_n\}$. Each cluster is determined by its centroid μ . Thus, the centroid μ_k of the cluster $C_k = \{I_1, I_2, \dots, I_{n_k}\}$ is defined in the following way:

$$\mu_k = \frac{\sum_{I_k \in C_k} I_k}{n_k} \quad (1)$$

The K-means-based segmentation searches for an optimal distribution of pixels to minimize the squared error between the empirical mean of the cluster and the respective points belonging to this cluster. This squared error between the cluster's centroid μ_k and arbitrary point belonging to the cluster C_k is defined as follows:

$$J(C_k) = \sum_{I_k \in C_k} \|I_k - \mu_k\|^2 \quad (2)$$

By this way, the K-means clustering minimizes the squared error over all the n clusters based on the equation:

$$J(C_k) = \sum_{k=1}^n \sum_{I_k \in C_k} \|I_k - \mu_k\|^2 \quad (3)$$

The K-means algorithm can be summarized into the following steps:

- Definition of the initial partitioning of the pixels into n clusters. Consequently, the next two steps are repeated until algorithm does not reach a convergence.
- Then algorithm then defines the further partitioning based on the pixel's assignment to the closest cluster's centroid.
- New clusters are recomputed.

4.2. Genetic Optimization of K-Means Clustering

In this section, we introduce a genetic optimization of the K-means clustering based on the modified ABC algorithm with improved searching strategy. The K-means clustering achieves the

convergence relatively fast. On the other hand, the main limitation of this approach is the initial phase where pixels are firstly grouped into individual classes. The farther from the real centroids the initial centroids are placed, the worse partitioning is achieved. It may result in inaccurate modelling of the thermal features, which are badly interpreted in the segmentation model. It is important to realize that there is not a uniformly-applicable approach for the initial placement of the centroids. Because of this, different image data acquired by various devices have different intensity features. These facts may significantly influence pixels' distribution, thus segmentation results may be sensitive against such phenomena. Furthermore, we must consider the image noise, which also may significantly influence the clustering accuracy. Based on these facts, the initial phase of the K-means should be optimized to improve the segmentation accuracy.

4.3. Proposal of Modified ABC Algorithm

The optimization process generated by the ABC algorithm is utilized for optimal distribution of the clusters representing significant facial thermal areas. This initial step predetermines an efficiency and robustness of the proposed model for alcohol intoxication. In the ABC algorithm, there are three groups of artificial bees, which are classified as: employed bees (EB), onlooker bees (OB), and scout bees (SB).

The first step of the ABC algorithm deals with generating of the initial population of food sources (SN) representing a set of possible solutions for the initial distribution of the centroids. In the conventional ABC, this step is done randomly. We take advantage a fact that the centroids are supposed to be defined in surrounding of the histogram peaks representing spots with high and concentrated intensity values. Thus, initial set of the food sources X_i (SN) is given by the equation:

$$X_i = R_{i,n} * E_n \quad (4)$$

where $R_{i,n} \in [0; 1]$ represents a vector of random number, ascended ordered to satisfy the condition: $0 \leq R_{i,1} \leq R_{i,2} \leq \dots \leq R_{i,n-1} \leq R_{i,n} \leq 1$ and E_n stands for a vector representing n the most significant peaks of the IR image histogram. We use a finite interval for the random numbers $R_{i,n}$ due to histogram normalization: $I[0, 255] \rightarrow I[0, 1]$. The term $I[0, 255]$ stands for 256 shade levels of the IR images. In the EB phase, we define for each X_i alternative surrounding solution V_i which is defined by the following way:

$$V_{i,k} = X_{\text{best}(i),k} + \phi_{i,k}(X_{r1,k} - X_{r2,k}) \quad (5)$$

In this equation, the index $k \in \{1, 2, \dots, n\}$ is randomly chosen from a number of centroids, $\phi_{i,k} \in [0; 1]$ stands for a random number and parameters $r1, r2 \in \{1, 2, \dots, SN\}$ represent mutually selected integers. A crucial element in this equation is the randomly chosen solution $X_{\text{best}(i),k}$. For each index k , we randomly select $p\%$ food sources X_i , where we select k^{th} centroid of such X_i satisfying the following condition: $X_{\text{best}(i),k}^P = \max_{\forall k \in n} \{fit_{X_{r1}}, fit_{X_{r2}}, \dots, fit_{X_{rl}}\}$. In this expression, the $fit_{X_{rl}}$ represents the fitness function of the l^{th} randomly selected X_i .

Since X_i and respective V_i are determined, their fitness functions are compared. If $fit_{X_i} < fit_{V_i}$ than algorithm keeps V_i as better solution, otherwise a new V_i is generated within a selected number of iterations, called the selection limit S_l . We use $S_l = 15$. After reaching this limit, the respective X_i is perceived as exhausted X_i^e , and eliminated from the memory.

In the OB phase, the wheel choice selection is applied. It is supposed that $OB = EB$. Thus, if some X_i are identified, new V_i are generated until $OB = EB$. The respective i^{th} food source is randomly selected, depending on its fitness function. A higher fitness function predetermines a higher chance of selection. Each considered food source is given by the probabilistic value p_i given by the following way:

$$p_i = \frac{fit_i}{\sum_{i=1}^{SN} fit_i} \quad (6)$$

A selected X_i is also compared with the V_i , as in the previous phase. Note that a higher fit_i corresponds with a higher probability p_i thus, better solution. A food source with the highest p_i is selected as the most suitable for the multiregional segmentation.

Lastly, the SB phase is employed. The scouts identify the exhausted food sources X_i^e . Instead of such food sources, the new are generated (Equation (7)), and the process of evolution is repeated.

$$X_{i,k} = X_{\min,j} + \text{rand}(0,1)(X_{\max,k} + X_{\min,k}) \quad (7)$$

where $i = \{1, 2, \dots, SN\}$ and $k = \{1, 2, \dots, n\}$.

The modified ABC Algorithm 1 is defined as follows:

Algorithm 1. Modified ABC Algorithm

Definition of initial parameters: number of food sources (SN), $p\%$ food sources X_i , number of iterations (It), selection limit (S_l), $\text{trial}_i = 0$ and number of centroids (n).

- Step 1: Generate the initial population of solutions X_i (e.g., 4).
 - Step 2: Calculate the population
 - Step 3: Iteration = 1
 - Step 4: Repeat
 - Step 5: Employed Bee Phase (EB)
 - Step 6: Generate new solutions for the employed bees.
 - Step 7: For $I = 1$ to SN do
 - Step 8: For each randomly selected $k \in \{1, 2, \dots, n\}$
 - Step 9: Randomly select $p\%$ food sources X_i
 - Step 10: Define $X_{\text{best}(i),k}^p$
 - Step 11: Define k^{th} element of the alternative solution V_i .
 - Step 12: end for
 - Step 13: end for
 - Step 14: if $\text{fit}_{X_i} < \text{fit}_{V_i}$ then
 - Step 15: Keep V_i as a better solution.
 - Step 16: Otherwise define a new V_i within a predefined S_l .
 - Step 17: After reaching this limit, X_i is transformed into exhausted X_i^e .
 - Step 18: end if
 - Step 19: Onlooker Bee Phase (OB)
 - Step 20: if $OB < EB$ then
 - Step 21: Define new X_i .
 - Step 22: end if
 - Step 23: until ($OB = EB$)
 - Step 24: Evaluate the probability p_i (e.g., 6) in order to evaluate a better solution defined by the fitness function.
 - Step 25: $P = 0$ and $I = 1$
 - Step 26: Repeat
 - Step 27: if random p_i is selected then
 - Step 28: Apply a greedy procedure between X_i and V_i , and consequently select the superior one.
 - Step 29: if X_i is not modified then
 - Step 30: $\text{trial}_i = \text{trial}_i + 1$
 - Step 31: otherwise $\text{trial}_i = 0$
 - Step 32: $p = p + 1$
 - Step 33: end if
 - Step 34: end if
 - Step 35: until ($p = SN$)
 - Step 36: Scout Bee Phase (SB)
 - Step 37: if exhausted X_i^e are identified then
 - Step 38: Define new X_i by the Equation (7), and repeat evaluation process.
 - Step 39: end if
 - Step 40: Remember the best fitness so far.
 - Step 41: Iteration = iteration+1
 - Step 42: until (iteration = max number of iterations)
 - Step 43: Select a food source with the highest fitness, which represent the initial centroids distribution.
-

4.4. Design of Fitness Function

Fitness function stands for a key element in the entire optimization process. The fitness function globally evaluates individual solutions and decides which is more suitable. Firstly, we define an objective function $J(C_k)$ evaluating statistical features in the respective segmentation class (cluster). Here, we suppose that the intensity spectrum inside any cluster should be concentrated without significant intensity variations. This assumption takes into advantage proximal similarity of the thermal features. A cluster which is less concentrated contains intensity values which have dissimilar features, thus the segmentation model is not consistent. The similarity of the intensity values can be measured by the statistical variance by the following way:

$$J(C_k) = \sum_{i=1}^n \sum_{j=1}^m \frac{1}{m} (I_j - \mu_n)^2, \forall I_j \in C(\mu_n) \quad (8)$$

and the fitness function is defined as follows:

$$fit_i = \frac{1}{1 + J(C_k)} \quad (9)$$

The evolution process of the objective function can be tracked by the convergence characteristics (Figures 4 and 5) showing the average and best objective values for each iteration. We report two stages of the testing of the objective function. Firstly, we report the convergence characteristics for the initial population: $SN = 80$ (Figure 4), and for $SN = 200$ (Figure 5). Both tests are performed for the number of iterations: {50, 80, 100, 150}. All the testing are performed for the IR images with the resolution 640×480 px.

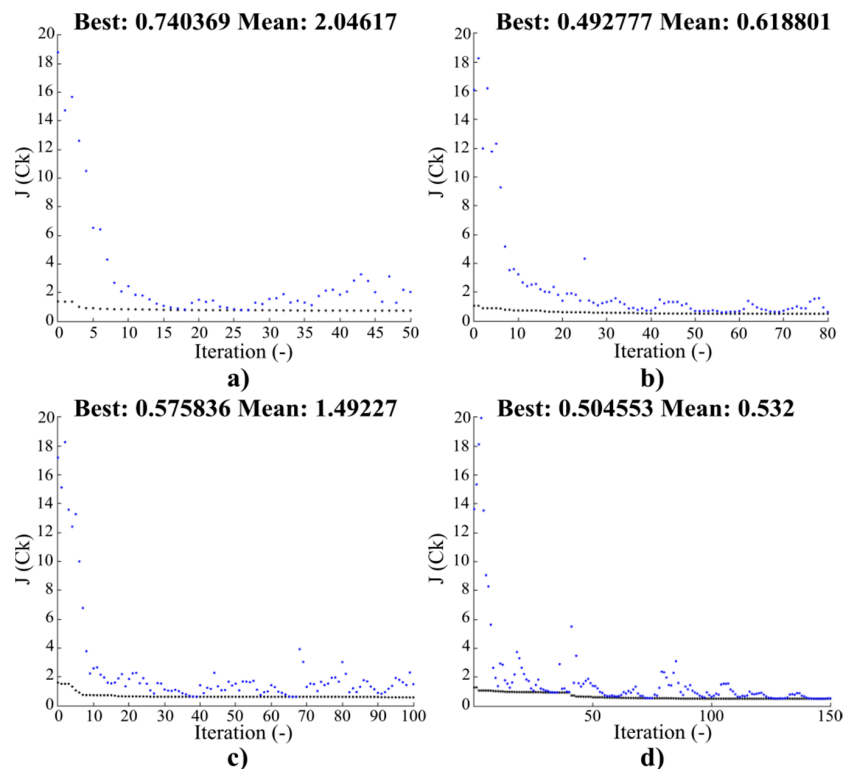


Figure 4. Convergence characteristics for the objective function $J(C_k)$ for the initial population $SN = 80$: (a) 50, (b) 80, (c) 100, and (d) 150 iterations.

Consequently, we test and compare the objective function for different IR image size. We gradually modify a size of the image resolution for the following sequence: $\{640 \times 480, 500 \times 500, 300 \times 300, 50 \times 50\}$. In the Tables 5–8, we report the average and best results of $J(C_k)$, $SN =$

100, $I_t = 50$, $p = 20\%$, and $S_1 = 15$ for three tested persons within alcohol intoxication. Based on the experimental result the objective function is getting increased when resizing original IR images. Such fact leads to a higher dispersion of the pixel intensities in individual clusters.

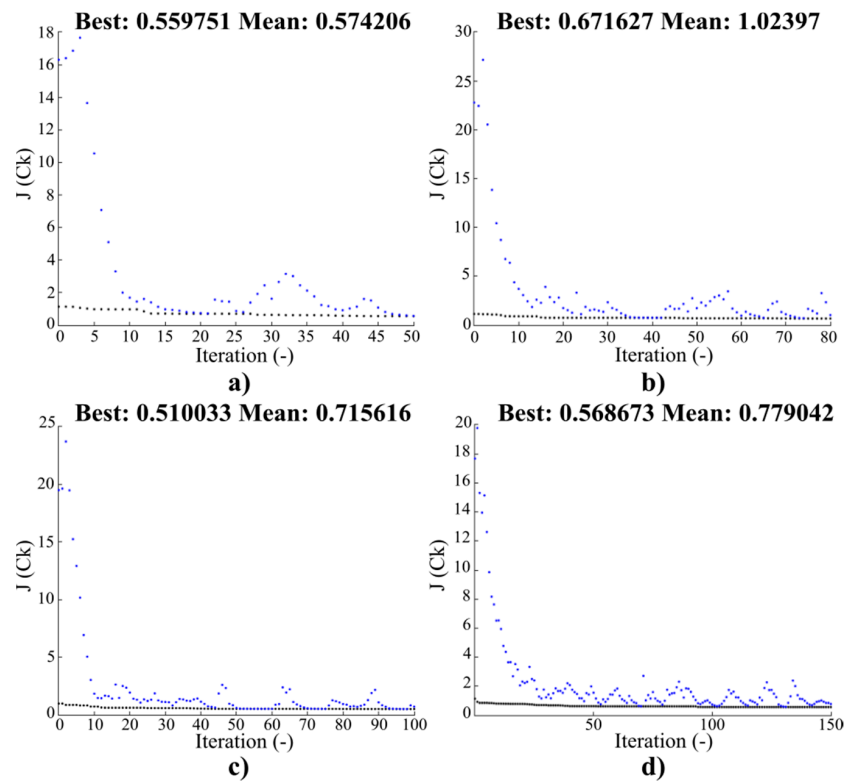


Figure 5. Convergence characteristics for the objective function $J(C_k)$ for the initial population $SN = 200$: (a) 50, (b) 80, (c) 100, and (d) 150 iterations.

Table 5. The average and best values for the objective function $J(C_k)$ for three tested persons within the gradual alcohol intoxication. Testing for the image resolution: 640×480 px.

Alcohol Content	Area of Interest	Best $J(C_k)$	Average $J(C_k)$	Best $J(C_k)$	Average $J(C_k)$	Best $J(C_k)$	Average $J(C_k)$
		Person 1		Person 2		Person 3	
Sober state	Nose	1.45	1.82	0.27	0.43	0.24	0.24
	Forehead	3.49	8.74	0.52	1.22	0.10	0.36
40 mL	Nose	1.54	1.55	0.32	0.84	0.27	0.58
	Forehead	2.98	7.67	0.45	0.56	0.27	0.33
80 mL	Nose	1.15	1.54	0.34	0.82	0.26	0.96
	Forehead	2.45	8.00	0.48	1.12	0.43	1.66
120 mL	Nose	1.47	5.20	0.29	0.62	0.29	0.38
	Forehead	3.33	7.66	0.57	1.51	0.66	0.69
160 mL	Nose	0.88	1.90	0.29	0.39	0.27	0.36
	Forehead	2.92	10.14	0.53	1.03	0.55	1.27

Table 6. The average and best values for the objective function $J(C_k)$ for three tested persons within the gradual alcohol intoxication. Testing for the image resolution: 500×500 px.

Alcohol Content	Area of Interest	Best $J(C_k)$	Average $J(C_k)$	Best $J(C_k)$	Average $J(C_k)$	Best $J(C_k)$	Average $J(C_k)$
		Person 1		Person 2		Person 3	
Sober state	Nose	1.62	1.87	0.38	0.42	0.28	0.25
	Forehead	3.55	9.12	0.74	1.25	0.17	0.38

Table 6. Cont.

Alcohol Content	Area of Interest	Best $J(C_k)$	Average $J(C_k)$	Best $J(C_k)$	Average $J(C_k)$	Best $J(C_k)$	Average $J(C_k)$
		Person 1		Person 2		Person 3	
40 mL	Nose	1.67	1.69	0.39	0.84	0.28	0.63
	Forehead	3.12	7.87	0.84	0.92	0.32	0.41
80 mL	Nose	1.17	1.64	0.41	0.64	0.32	1.14
	Forehead	2.55	8.57	0.52	1.18	0.47	1.84
120 mL	Nose	1.69	5.28	0.36	0.69	0.51	0.78
	Forehead	3.87	7.69	0.61	1.67	0.69	0.84
160 mL	Nose	1.14	1.96	0.35	0.85	0.32	0.42
	Forehead	2.96	10.23	0.62	1.52	0.58	1.54

Table 7. The average and best values for the objective function $J(C_k)$ for three tested persons within the gradual alcohol intoxication. Testing for the image resolution: 300×300 px.

Alcohol Content	Area of Interest	Best $J(C_k)$	Average $J(C_k)$	Best $J(C_k)$	Average $J(C_k)$	Best $J(C_k)$	Average $J(C_k)$
		Person 1		Person 2		Person 3	
Sober state	Nose	1.91	1.92	0.42	0.42	0.33	0.52
	Forehead	3.85	9.55	0.86	1.44	0.45	0.45
40 mL	Nose	1.59	1.67	0.41	0.92	0.32	0.71
	Forehead	3.51	8.01	0.92	1.62	0.45	0.45
80 mL	Nose	1.95	1.95	0.55	0.73	0.66	1.52
	Forehead	2.62	8.68	0.56	1.62	0.55	1.87
120 mL	Nose	1.74	5.36	0.45	0.76	0.58	0.65
	Forehead	3.92	7.74	0.66	1.84	0.74	0.89
160 mL	Nose	1.38	2.52	0.81	0.89	0.45	0.52
	Forehead	3.15	10.44	0.71	1.68	0.99	1.66

Table 8. The average and best values for the objective function $J(C_k)$ for three tested persons within the gradual alcohol intoxication. Testing for the image resolution: 50×50 px.

Alcohol Content	Area of Interest	Best $J(C_k)$	Average $J(C_k)$	Best $J(C_k)$	Average $J(C_k)$	Best $J(C_k)$	Average $J(C_k)$
		Person 1		Person 2		Person 3	
Sober state	Nose	2.45	2.54	1.84	1.22	1.12	1.42
	Forehead	4.55	10.84	1.65	1.49	1.35	1.92
40 mL	Nose	1.95	2.45	1.42	1.57	1.12	1.74
	Forehead	3.84	8.63	1.38	1.63	1.65	1.95
80 mL	Nose	2.21	2.45	1.69	1.91	1.31	1.69
	Forehead	2.93	8.99	1.31	1.87	1.43	1.92
120 mL	Nose	2.62	6.41	1.41	1.85	1.31	1.45
	Forehead	4.81	7.84	1.56	2.32	1.36	1.89
160 mL	Nose	1.83	2.76	1.21	1.84	1.12	1.52
	Forehead	3.94	11.13	1.62	2.37	1.63	2.52

5. Experimental Results and Evaluation

In this section, we introduce experimental results of the IR facial modeling of alcohol intoxication. Modeling of alcohol intoxication is done in all twenty volunteers, while we report, in this section, three cases for different segmentation settings. We suppose that the coldest area in the nose will reduce, while the hottest intensity spectrum in the forehead will expand, whilst drinking alcohol. The proposed multiregional segmentation enables identification of finite clusters, grouping intensity values with similar features. The number of segmentation classes is an important parameter in controlling

partitioning of the facial thermal map. In our analysis, we compare different number of clusters to obtain an optimal cluster setting, which will reflect temperature variations caused by alcohol intoxication. We report a comparison for 3 (Figures 6 and 7), 8 (Figures 8 and 9) and 11 (Figures 10 and 11) clusters. When comparing different numbers of segmentation clusters, we found out that lower numbers of the clusters (3 clusters) are not able to detect weaker temperature differences, and contrarily a higher number of the clusters lead to the noise presence in the segmentation model, exhibited by discontinuities in the segmentation map. Therefore, we experimentally set eight segmentation classes for the modelling. These settings appear as a good compromise, where facial temperature features are observable within the process of gradual intoxication. Each segmentation class is represented by a unique color, which enables visual differentiation of individual clusters. The coldest spectrum in the nose is indicated by the red class. Individual rows indicate gradual drinking process from the sober state (first up row) up to the maximal intoxication (first down row).

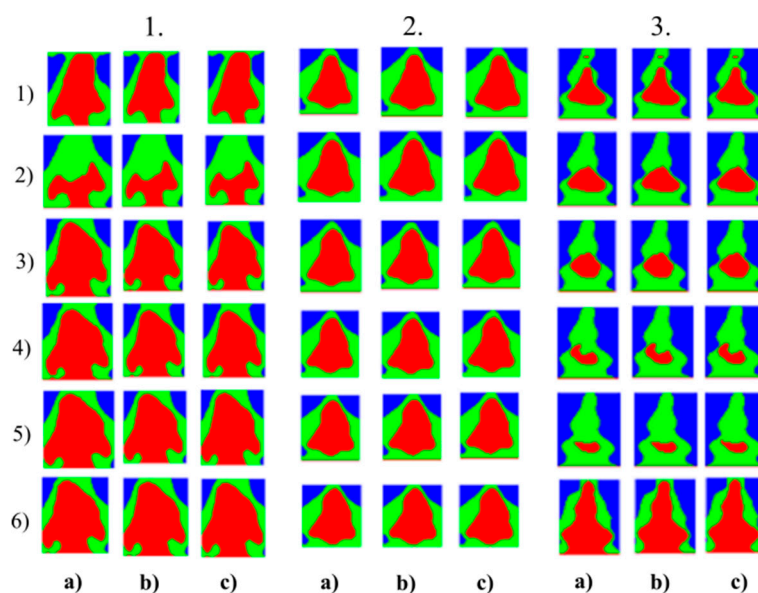


Figure 6. Multiregional segmentation with three clusters of the nose area for three tested persons for: (a) SN = 100, It = 100, (b) SN = 70, It = 90 and (c) SN = 120, It = 160. From the top, each row corresponds with gradual intoxication: (1) sober state, (2) 40 mL, (3) 80 mL, (4) 120 mL, (5) 160 mL, and (6) 200 mL.

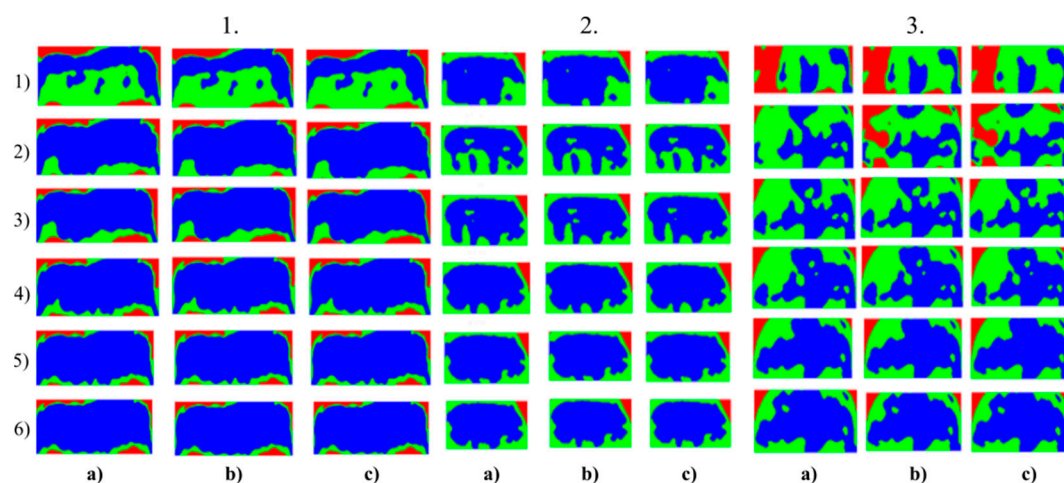


Figure 7. Multiregional segmentation with three clusters of the forehead area for three tested persons for: (a) SN = 100, It = 100, (b) SN = 70, It = 90, and (c) SN = 120, It = 160. From the top, each row corresponds with gradual intoxication: (1) sober state, (2) 40 mL, (3) 80 mL, (4) 120 mL, (5) 160 mL, and (6) 200 mL.

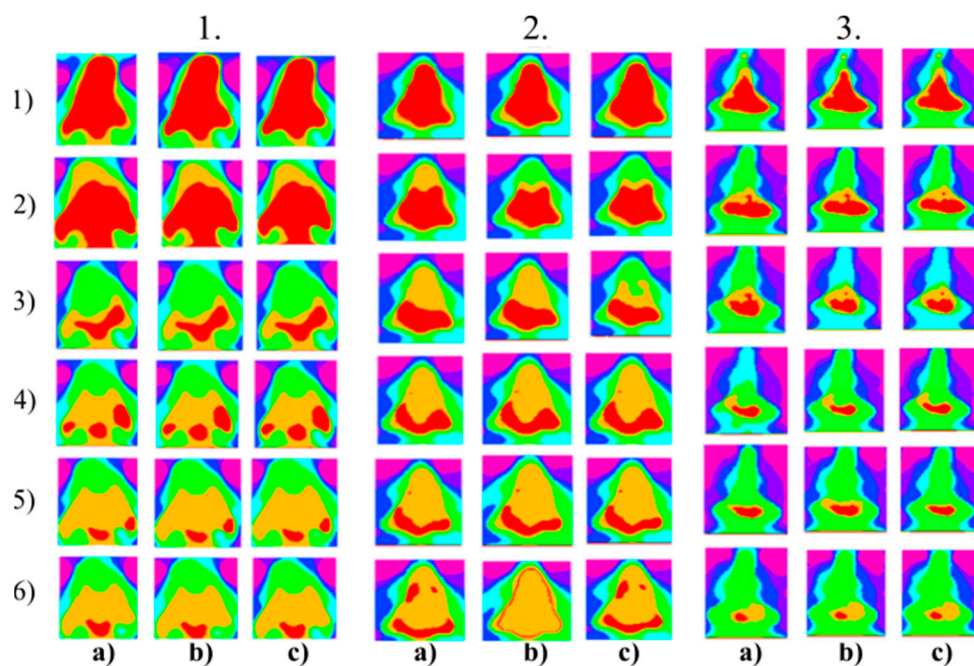


Figure 8. Multiregional segmentation with eight clusters of the nose area for three tested persons for: (a) SN = 100, It = 100, (b) SN = 70, It = 90 and (c) SN = 120, It = 160. From the top, each row corresponds with gradual intoxication: (1) Sober state, (2) 40 mL, (3) 80 mL, (4) 120 mL, (5) 160 mL, and (6) 200 mL.

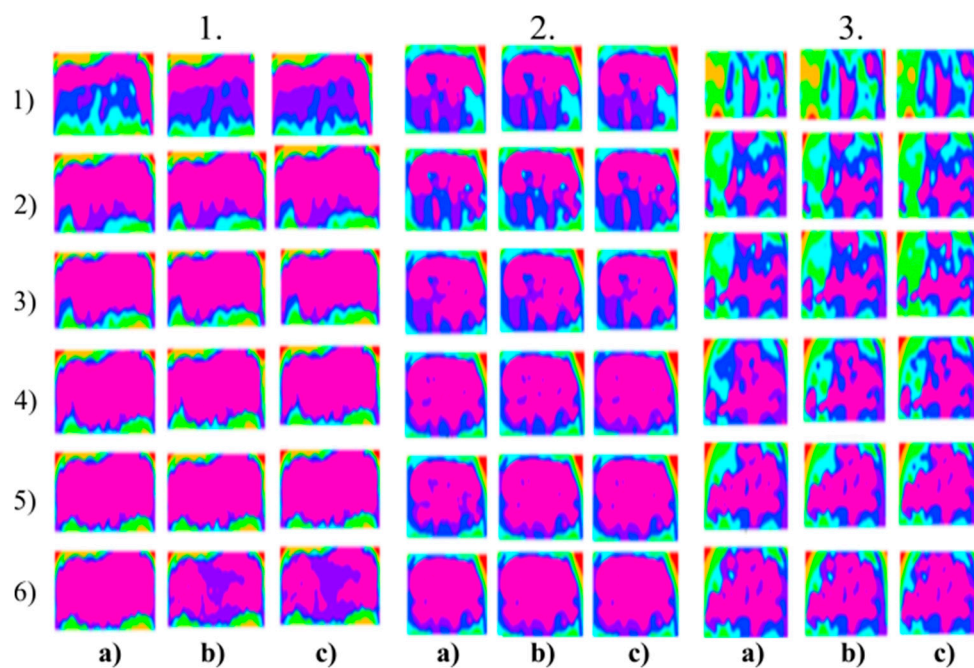


Figure 9. Multiregional segmentation with eight clusters of the forehead area for three tested persons for: (a) SN = 100, It = 100, (b) SN = 70, It = 90, and (c) SN = 120, It = 160. From the top, each row corresponds with gradual intoxication: (1) sober state, (2) 40 mL, (3) 80 mL, (4) 120 mL, (5) 160 mL, and (6) 200 mL.

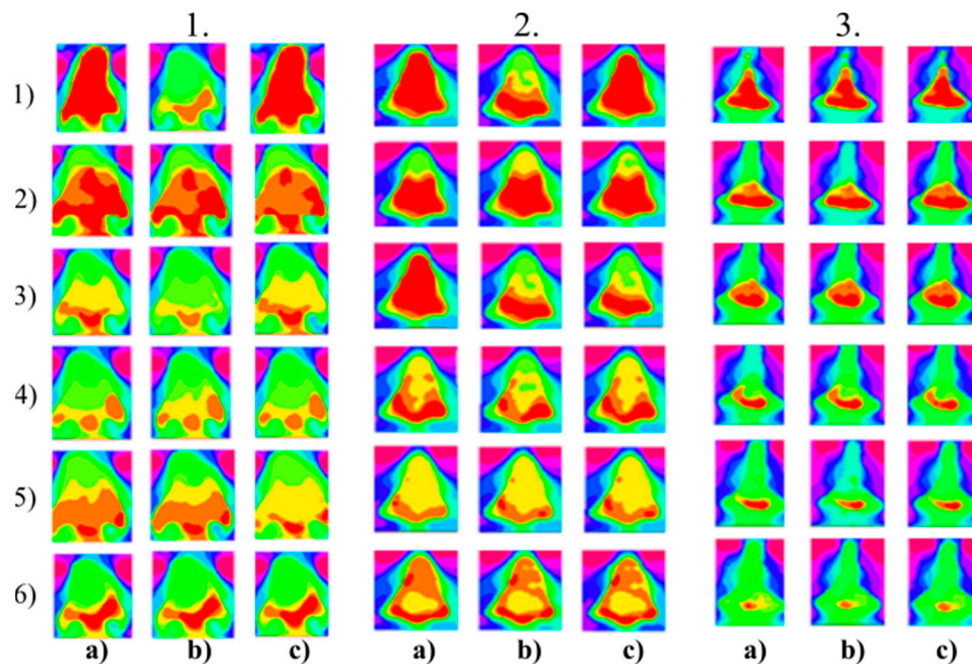


Figure 10. Multiregional segmentation with eleven clusters of the nose area for three tested persons for: (a) SN = 100, It = 100, (b) SN = 70, It = 90, and (c) SN = 120, It = 160. From the top, each row corresponds with gradual intoxication: (1) sober state, (2) 40 mL, (3) 80 mL, (4) 120 mL, (5) 160 mL, and (6) 200 mL.

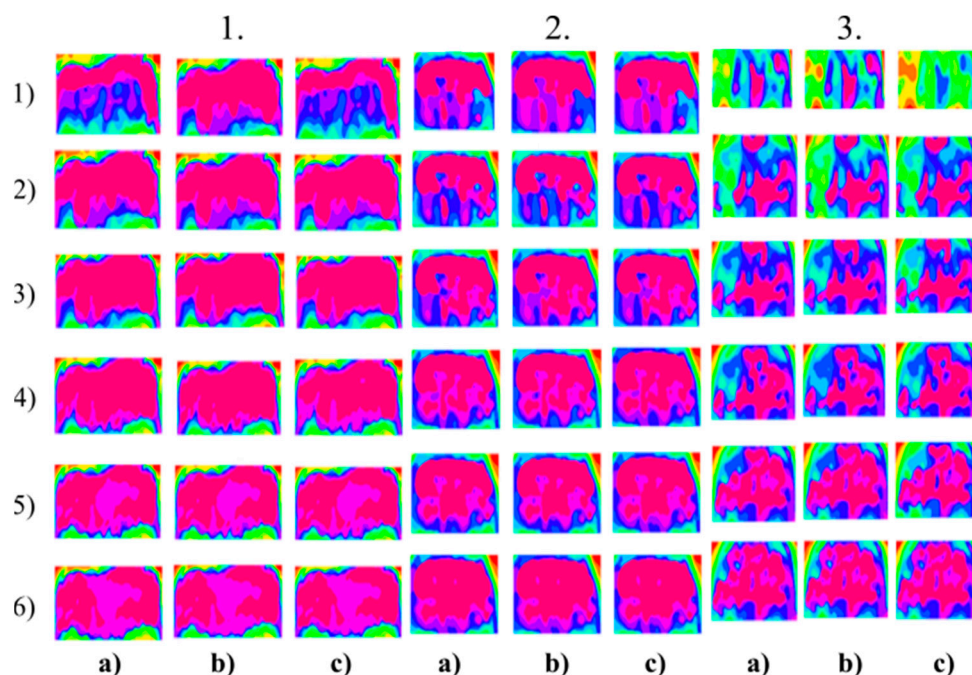


Figure 11. Multiregional segmentation with eleven clusters of the forehead area for three tested persons for: (a) SN = 100, It = 100, (b) SN = 70, It = 90, and (c) SN = 120, It = 160. From the top, each row corresponds with gradual intoxication: (1) sober state, (2) 40 mL, (3) 80 mL, (4) 120 mL, (5) 160 mL, and (6) 200 mL.

Based on the multiregional segmentation modelling, we identify a respective segmentation class representing the dynamical thermal features for the nose and forehead whilst alcohol consuming. The Figures 12 and 13 represent a resulting mathematical model in the binary form for the nose and

forehead area. We report the binary dynamical model for three persons. This model represents the dynamical descending trend for the coldest intensity area of the nose, and the increasing dynamical tendency of the hottest area for the forehead.

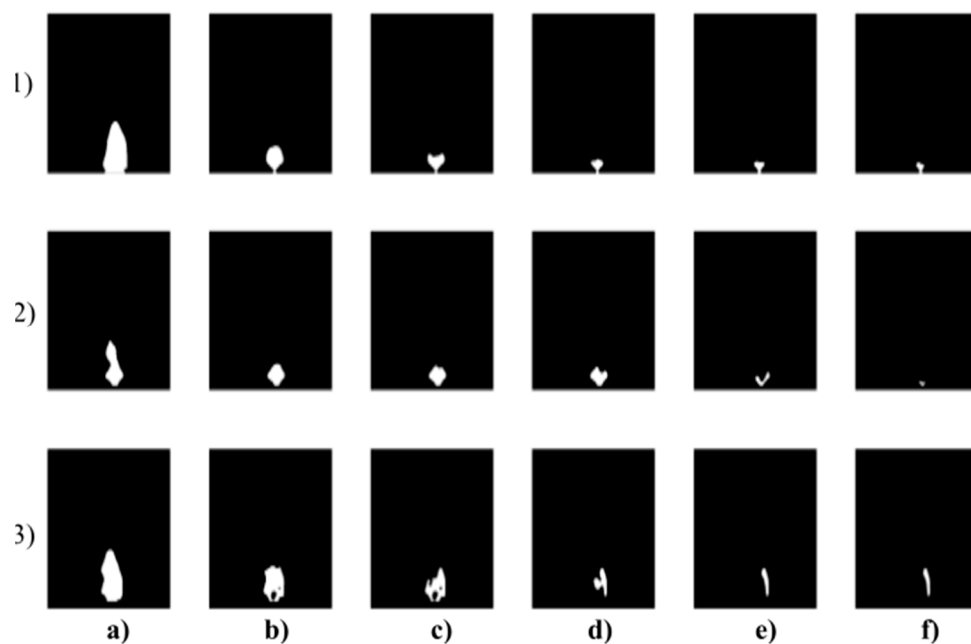


Figure 12. Binary modeling of the nose dynamical features for three persons (rows) where each column represents gradual alcohol intoxication: (a) Sober state, (b) 40 mL, (c) 80 mL, (d) 120 mL, (e) 160 mL, and (f) 200 mL of the alcohol.

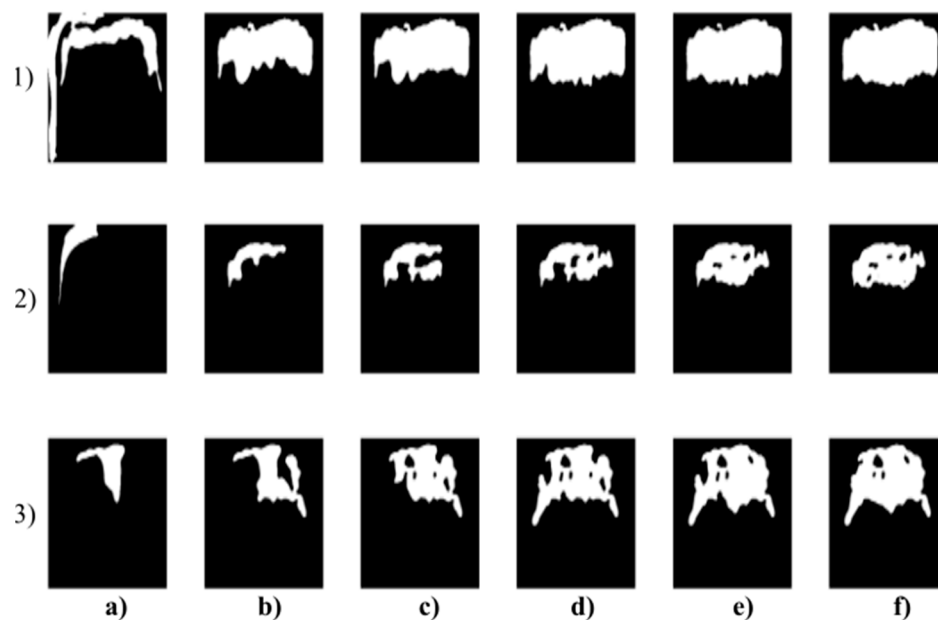


Figure 13. Binary modeling of the forehead dynamical features for three persons (rows) where each column represents gradual alcohol intoxication: (a) Sober state, (b) 40 mL, (c) 80 mL, (d) 120 mL, (e) 160 mL, and (f) 200 mL of the alcohol.

Based on the binary models, we can objectively measure trend of the dynamical features. Since we observe dynamical change of the area size of the model within the gradual alcohol intoxication, we measure this size expressed by a number of pixels. As an example, we report this dynamical feature for the nose area in the Figure 14.

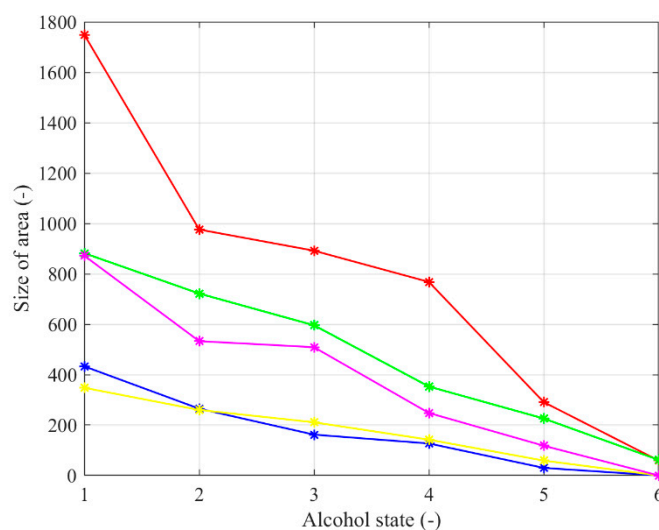


Figure 14. Averaged decreasing trend of the binary model size for the nose area of 5 tested persons.

An important part of the proposed segmentation model of alcohol intoxication is the validation with the real alcohol content. As we already stated, we do not directly measure the alcohol content in the human body, but an alcohol side effect causing facial temperature variations in the nose and forehead. Since facial temperature is related with the real alcohol content, we validate our results against results of the breath analysis. For the validation of the proposed model, we studied the correlation coefficient between the alcohol content measured by the breath analyzer and the nose and forehead area for individual stages of alcohol drinking. Figures 15 and 16 report result of this analysis for all twenty volunteers. We achieve relatively high correlation of the forehead in the range: $corr \in \langle 0.59; 0.98 \rangle$ and nose: $corr \in \langle 0.76; 0.99 \rangle$. The correlation in the nose is generally higher. This is supposedly caused by the hair, which may influence the temperature distribution.

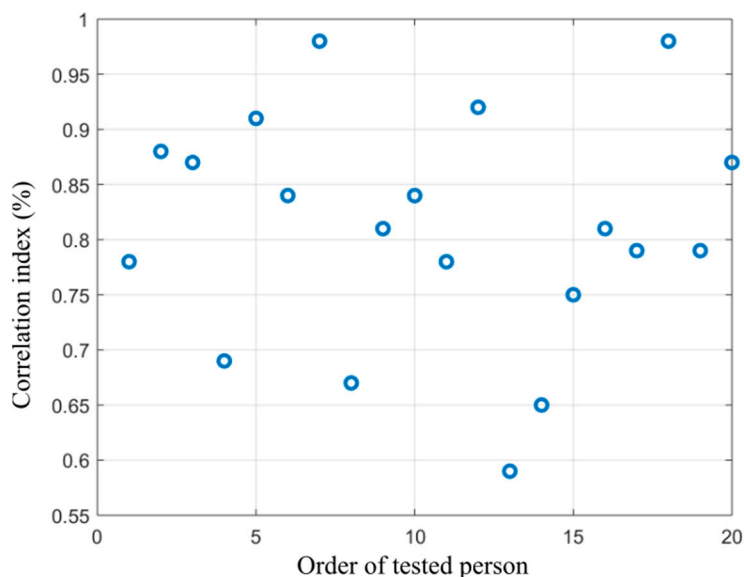


Figure 15. Distribution of correlation index showing dependency between the alcohol content measured from the breath and area size of the hottest area in the forehead calculated from the proposed segmentation model.

In the next step, we measure the computation time of the segmentation process depending on various optimization settings. Segmentation method is as effective, as works fast. In the Tables 9–11, we report the time complexity for various ABC settings.

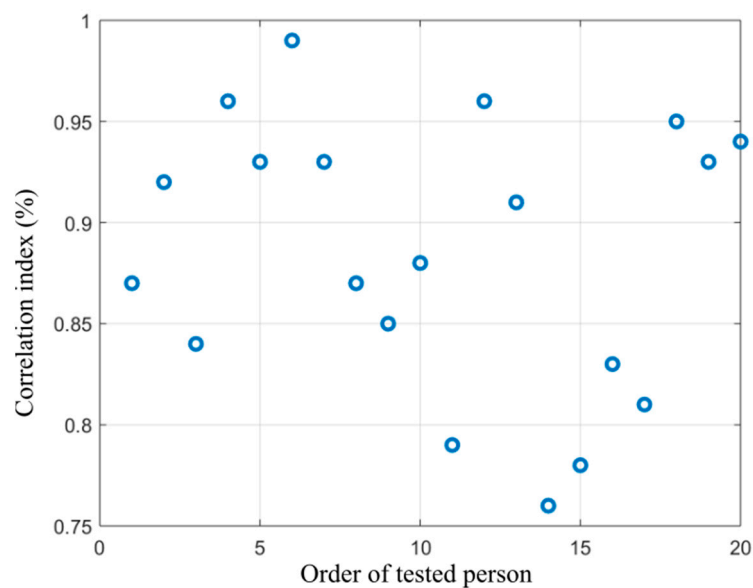


Figure 16. Distribution of correlation index showing dependency between the alcohol content measured from breath and area size of the coldest area in the nose calculated from the proposed segmentation model.

Table 9. Time complexity for eight segmentation classes, SN = 100 and It = 100, p = 20% and $S_1 = 15$.

Alcohol Content	Area of Interest	Time Complexity [s]		
		Person 1	Person 2	Person 3
Sober State	Nose	21.97	21.28	17.97
	Forehead	33.27	22.67	20.52
40 mL	Nose	23.66	19.41	17.02
	Forehead	35.48	18.03	20.97
80 mL	Nose	25.83	17.69	18.28
	Forehead	33.67	19.25	20.57
120 mL	Nose	23.01	18.89	19.57
	Forehead	35.89	20.78	19.41
160 mL	Nose	23.09	17.99	18.86
	Forehead	33.43	19.52	20.70
200 mL	Nose	25.87	17.33	18.75
	Forehead	31.87	18.37	19.62

Table 10. Time complexity for eight segmentation classes, SN = 70 and It = 90, p = 20%, and $S_1 = 15$.

Alcohol Content	Area of Interest	Time Complexity [s]		
		Person 1	Person 2	Person 3
Sober State	Nose	31.07	15.28	15.14
	Forehead	25.07	16.32	16.75
40 mL	Nose	16.96	15.15	15.97
	Forehead	26.14	17.20	15.41
80 mL	Nose	17.65	15.33	15.64
	Forehead	28.70	14.94	15.42
120 mL	Nose	18.72	14.86	14.98
	Forehead	30.72	15.42	16.70
160 mL	Nose	18.78	15.12	14.02
	Forehead	24.25	16.29	15.72
200 mL	Nose	16.20	15.72	14.83
	Forehead	25.07	15.33	17.16

Table 11. Time complexity for eight segmentation classes, SN = 120 and It = 60, p = 20%, and $S_1 = 15$.

Alcohol Content	Area of Interest	Time Complexity [s]		
		Person 1	Person 2	Person 3
Sober State	Nose	18.42	14.97	14.98
	Forehead	25.19	16.37	15.75
40 mL	Nose	18.89	14.88	14.58
	Forehead	26.93	15.24	15.43
80 mL	Nose	16.92	15.19	14.87
	Forehead	26.05	16.09	14.76
120 mL	Nose	17.49	14.47	14.96
	Forehead	25.83	16.26	14.97
160 mL	Nose	15.88	13.10	15.14
	Forehead	28.46	14.59	15.04
200 mL	Nose	17.11	14.06	14.21
	Forehead	24.48	15.49	16.78

6. Quantitative Comparison

In this section, we present a quantitative comparison against selected segmentation methods by using objective parameters enabling evaluation of the efficiency and robustness. We present quantitative comparison for the native IR images, as well as for IR images corrupted by the deterministic noise.

This analysis is done for all the twenty tested persons. For each image, the gold standard is defined manually. We consider the following scalar parameters for comparison:

Correlation coefficient (Corr) measures a level of the linear correlation between two samples. Corr gives values in the range $[0; 1]$ where 0 stands for no linear dependence, while 1 denotes totally identical samples.

Rand index (RI) brings a comparison of a compatibility of assignment between pairs of elements in two samples. RI gives results in $[0; 1]$. RI is defined by the following way:

$$RI(C_1, C_2) = \frac{2(n_{11} + n_{00})}{N(N-1)} \quad (10)$$

In the Equation (10), N stands for a total number of points, n_{11} represents number of pairs lying in the same area C_1 and C_2 and n_{00} is a number of pairs in different segmentation classes.

Variation of information (VI) measures a distance between two regions in the sense of their conditional entropy. The VI is defined as follows:

$$VI(C_1, C_2) = \mathcal{H}(C_1) + \mathcal{H}(C_2) - 2I(C_1, C_2) \quad (11)$$

In the Equation (11), $\mathcal{H}(C_p)$ represents an entropy associated with the region C_p and $I(C_1, C_2)$ stands for mutual information between regions C_1 and C_2 .

Mean Squared Error (MSE) measures the averaged error between two samples. This parameter is defined as follows:

$$MSE(C_1, C_2) = \frac{1}{N} \sum_{i=1}^N (C_2 - C_1)^2 \quad (12)$$

As alternative methods for a comparison, we use the multiregional Otsu segmentation, K-means, FCM clustering and region growing (RG) method (Table 12). We present a comparison for additive artificial deterministic Gaussian ($G(\mu, \sigma^2)$) in the Tables 13 and 14, Salt and Pepper (SaP(d)) in the Tables 15 and 16 and Multiplicative ($M(\mu, \sigma^2)$) noise in the Tables 17 and 18. The following tables show the testing results where the best results are highlighted. All the comparisons are done for the ABC settings: SN = 100, It = 100, p = 20% and $S_1 = 15$.

Table 12. Quantitative comparison for the native IR images (640×480 px).

	Proposed	Otsu	K-Means	FCM	RG
Corr	0.94	0.91	0.88	0.93	0.74
RI	0.91	0.88	0.81	0.92	0.71
VI	3.11	3.21	4.15	4.11	5.01
MSE	28.45	35.87	36.12	29.98	36.88

Table 13. Quantitative comparison for the Gaussian noise: $G(0, 0.05)$, (640×480 px).

	Proposed	Otsu	K-Means	FCM	RG
Corr	0.91	0.88	0.84	0.82	0.69
RI	0.91	0.82	0.75	0.87	0.66
VI	2.98	3.27	5.11	4.52	5.44
MSE	31.52	34.57	33.18	31.99	38.74

Table 14. Quantitative comparison for the Gaussian noise: $G(0, 0.8)$, (640×480 px).

	Proposed	Otsu	K-Means	FCM	RG
Corr	0.88	0.75	0.81	0.69	0.48
RI	0.74	0.76	0.45	0.66	0.43
VI	3.87	4.12	5.56	4.75	7.57
MSE	33.87	36.88	34.12	35.41	39.45

Table 15. Quantitative comparison for the Salt and Pepper noise: $SaP(0.04)$, (640×480 px).

	Proposed	Otsu	K-Means	FCM	RG
Corr	0.93	0.79	0.86	0.88	0.69
RI	0.91	0.93	0.88	0.91	0.66
VI	3.54	4.18	5.48	4.12	6.55
MSE	28.45	30.12	31.15	34.47	36.84

Table 16. Quantitative comparison for the Salt and Pepper noise: $SaP(0.9)$, (640×480 px).

	Proposed	Otsu	K-Means	FCM	RG
Corr	0.79	0.65	0.66	0.71	0.38
RI	0.84	0.83	0.75	0.74	0.41
VI	5.12	5.99	7.84	6.12	6.77
MSE	33.54	31.85	33.45	33.32	39.85

Table 17. Quantitative comparison for the Multiplicative noise: $M(0, 0.03)$, (640×480 px).

	Proposed	Otsu	K-Means	FCM	RG
Corr	0.88	0.78	0.69	0.76	0.64
RI	0.91	0.82	0.83	0.79	0.68
VI	2.99	3.21	5.34	4.63	7.11
MSE	32.84	32.65	34.56	36.93	41.12

Table 18. Quantitative comparison for the Multiplicative noise: $M(0, 0.6)$, (640×480 px).

	Proposed	Otsu	K-Means	FCM	RG
Corr	0.74	0.68	0.61	0.59	0.48
RI	0.75	0.74	0.81	0.54	0.48
VI	3.16	3.93	5.91	5.17	8.15
MSE	33.54	32.89	36.45	39.62	44.19

The best results indicate that the proposed clustering scheme driven by the modified ABC algorithm shows the most robust results, even if comparing with the noisy images. Noise is important aspect which should always be considered. Also, an important issue is the model's features representing and quantifying the gradual alcohol drinking. Therefore, for the proposed algorithm we measure the trend development for gradual drinking for native images in a comparison with individual noise parameters. As is obvious, the results are only slightly different. This fact indicates a higher level of robustness of the proposed method against additive noise.

Firstly, we analyze the Gaussian noise. The Figure 17 shows different parameters of the Gaussian noise and the Figure 18 trend characteristics for the Gaussian noise. It is the most frequent type of the noise. It is characterized by the normal distribution causing equal deterioration of the pixels. It means that a level of the noise does not depend of the pixel intensity value. In the Gaussian noise, we set the variance and mean value $G(\mu, \sigma^2)$.

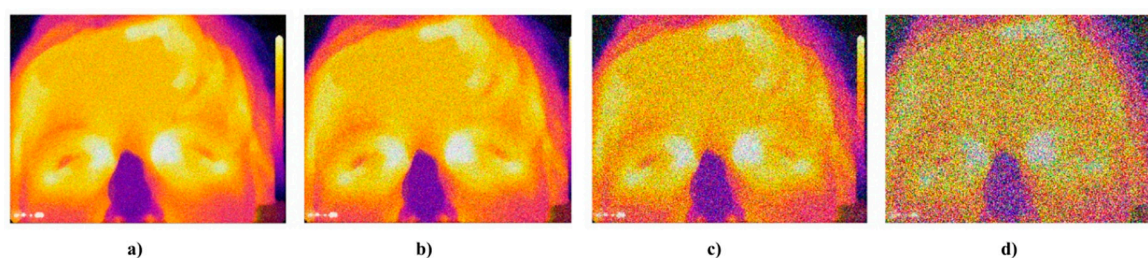


Figure 17. Example of IR facial images corrupted by the Gaussian noise: (a) $G(0, 0.01)$, (b) $G(0, 0.07)$, (c) $G(0, 0.3)$, and (d) $G(0, 0.5)$.

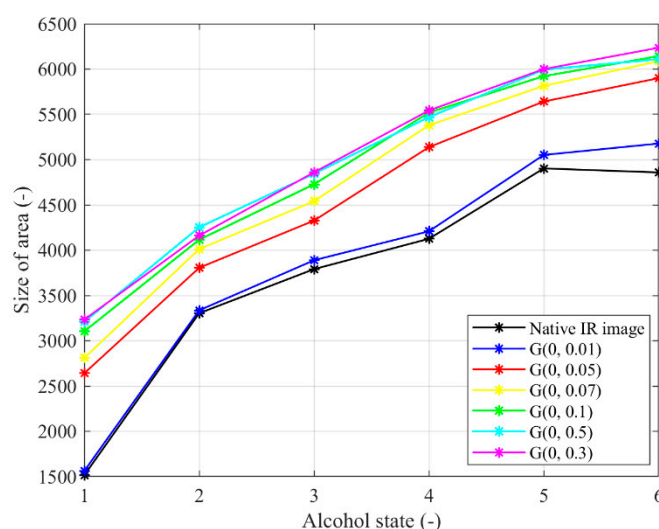


Figure 18. Trend characteristic for Gaussian noise $G(\mu, \sigma^2)$ with different settings $\mu = 0$, $\sigma^2 = \{0.01, 0.05, 0.07, 0.1, 0.3, 0.5\}$.

Here, we report results of the Salt and Pepper noise. This noise has binary representation. The salt and pepper noise is controlled by its density $SaP(d)$. Figure 19 reports results of this noise for $d = \{0.01, 0.05, 0.07, 0.5\}$, while Figure 20 reports the trend characteristic for the salt and pepper noise.

Lastly, we report results of the multiplicative noise $M(\mu, \sigma^2)$, which is represented by the granulated texture (Figure 21). This type of the noise is typical for ultrasound imaging and is generally caused by improper transfer of the image data. It is not caused by random electrical noise but is related with detector settings. We report the IR images corrupted by the multiplicative noise with parameters $\mu = 0$, $\sigma^2 = \{0.01, 0.05, 0.3, 0.5\}$ (Figure 21), while the Figure 22 reports the trend characteristics for the multiplicative noise.

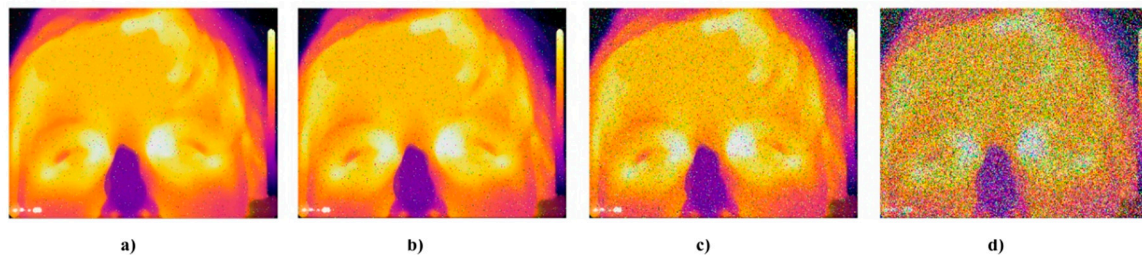


Figure 19. Example of IR facial images corrupted by the Salt and Pepper: (a) SaP(0.01), (b) SaP(0.05), (c) SaP(0.07), and (d) SaP(0.5).

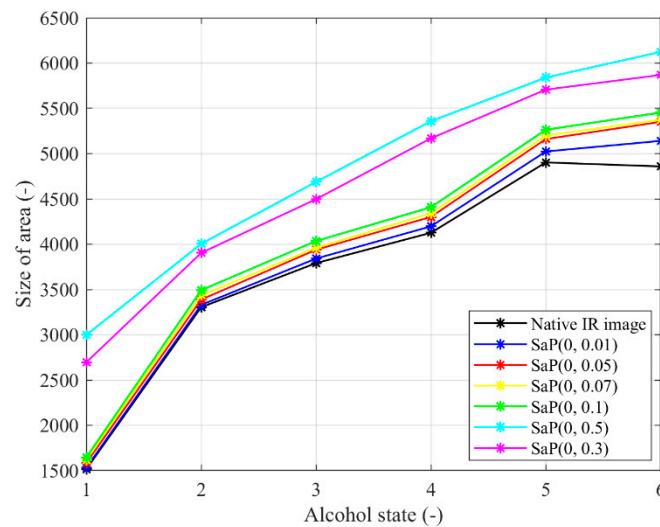


Figure 20. Trend characteristic for the salt and pepper noise SaP(d) with different density settings: $d = \{0.01, 0.05, 0.07, 0.1, 0.3, 0.5\}$.

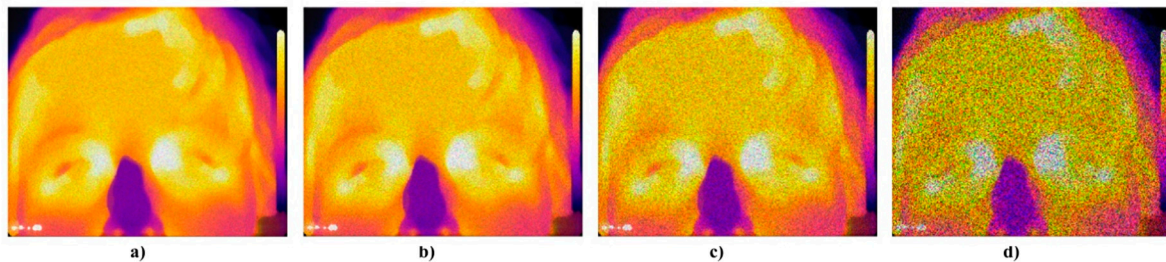


Figure 21. Example of IR facial images corrupted by the salt and pepper: (a) $\mu = 0$, $\sigma^2 = 0.01$, (b) $\mu = 0$, $\sigma^2 = 0.05$, (c) $\mu = 0$, $\sigma^2 = 0.3$, and (d) $\mu = 0$, $\sigma^2 = 0.5$.

Lastly, we perform the analysis of the modified ABC algorithm against selected conventional evolutionary schemes. The entire tested algorithms are implemented with the goal of a definition of the initial clusters for the K-means method. All the testing is done for 8 segmentation classes, and image resolution: 640×480 px. We select for a comparison Artificial Bee Colony (ABC), Particle Swarm Optimization (PSO) and GA algorithm. All these optimization procedures are tested for same IR images as the proposed modified ABC algorithm. Tables 19–21 represent experimental evolutionary algorithm settings used for the comparative analysis. Details of the evolutionary optimization settings can be found in [41]. For the alternative optimization methods settings (Tables 19–22), we use recommendations from [41]. We tested all the optimization settings for IR image segmentation from Tables 19–22. In the objective evaluation (Tables 23–25), we report the best results for each method. All the experimental testing is done on the sample of twenty volunteers (nose and forehead IR images),

together we analyze $n = 40$ IR images. The following parameters of the mentioned optimization methods are considered for the comparison.

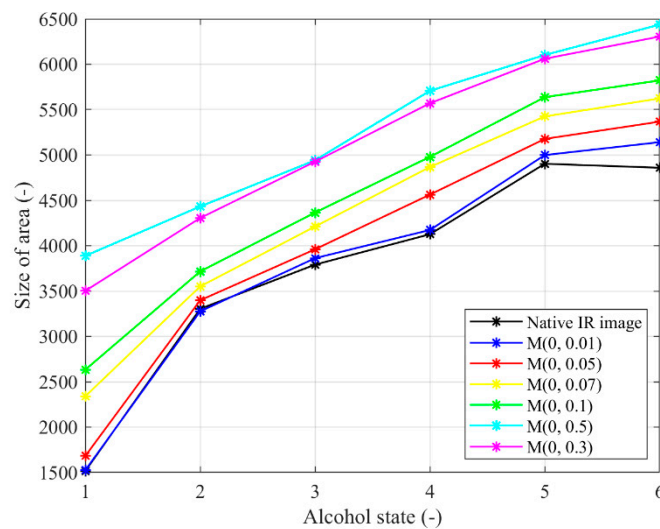


Figure 22. Trend characteristic for the Multiplicative noise $M(\mu, \sigma^2)$ with different settings: $\mu = 0, \sigma^2 = \{0.01, 0.05, 0.07, 0.1, 0.3, 0.5\}$.

Table 19. Parameters settings for the modified Artificial Bee Colony (ABC) algorithm.

Parameter	Value
Number of food sources (SN)	{80, 100, 200, 500}
Number of iterations (It)	{50, 100, 300, 500}
selection limit (S_l)	{10, 15}
Lower limitation (X_{\min}) and upper limitation (X_{\max})	(0, 1)

Table 20. Parameters settings for the ABC algorithm.

Parameter	Value
Number of food sources (SN)	{80, 100, 200, 500}
Number of iterations (It)	{50, 100, 300, 500}
selection limit (S_l)	{10, 15}
Lower limitation (X_{\min}) and upper limitation (X_{\max})	(0, 1)

Table 21. Parameters settings for the Particle Swarm Optimization (PSO) algorithm.

Parameter	Value
Swarm size	{80, 100, 200, 500}
Number of iterations (It)	{50, 100, 300, 500}
Cognitive, social and neighborhood acceleration	{2, 1, 3}
Lower limitation (W_{\min}) and upper limitation (W_{\max})	(0, 255)
Error goal	1×10^{-6}
Maximal trial limit	450
Value of velocity weight at the end of the PSO iterations	0.3
Value of velocity weight at the beginning of the PSO	0.97
The fraction of the maximum iterations, for which W is linear evolved	0.6
Value of global minimum	0

Table 22. Parameters settings for the GA.

Parameter	Value
Population size	{80, 100, 200, 500}
Number of iterations (It)	{50, 100, 300, 500}
Crossover probability	{0.2, 0.4, 0.5}
Mutation probability	{0.1, 0.3, 0.5}
Number of bits for each variable	7
Eta (η)	1
Lower limitation (X_{\min}) and upper limitation (X_{\max})	(0, 1)

For the objective comparison of effectivity of the modified ABC algorithm against alternative optimization strategies, we consider the following parameters:

Peak Signal-to-Noise Ratio (PSNR) [dB] expresses a ratio between the maximal power of the signal and the corrupting noise [42–44]. By using the Mean Squared Error (MSE), the PSNR is defined as follows:

$$\text{PSNR} = 10 \log_{10} \left(\frac{\text{MAX}_I^2}{\text{MSE}} \right) \quad (13)$$

In this expression, MAX_I stands for the maximal pixel's intensity value. We analyze 8-bit IR images, so $\text{MAX}_I = 255$.

Structural Similarity index (SSIM) is a parameter that predicts quality of the digital image [45–48]. SSIM is used for assessment and measurement of similarities between two images. Having two images (gold standard and tested image) denoted as x and y , the SSIM is calculated as follows:

$$\text{SSIM}(x, y) = \frac{(2\mu_x\mu_y + c_1)(2\sigma_{xy} + c_2)}{(\mu_x^2 + \mu_y^2 + c_1)(\sigma_x^2 + \sigma_y^2 + c_2)} \quad (14)$$

where μ stands for the average, σ^2 is the variance, σ_{xy} is the covariance of x and y .

Feature Similarity index (FSIM) contains two stages: Phase congruency (PC), which a dimensionless quantity of the significance of a local structure map. This stage is considered as a primary feature in the FSIM. The second used feature is the image Gradient Magnitude (GM). These two features in the FSIM are complementary of each other regarding specifying the image local quality [49–53].

For all the tested methods, we selected such settings from the Tables 19–22 which reflect the best results of the stated parameters. For each image resolution: $\{640 \times 480, 500 \times 500, 300 \times 300, 50 \times 50\}$, we report five images with the best results. The best result for each test is highlighted.

Table 23 reports results from the experimental testing of the PSNR for different resolution. PSNR. This parameter takes the MSE as indicator of the segmentation variability (13) regarding to the gold standard. The lower MSE we obtain, the higher similarity we obtain for segmentation model. Based on the results (Table 23), we can deduce that the image resolution significantly reduces this parameter. Thus, the image resolution has a substantial impact on the segmentation effectivity.

Second considered parameter is the structural similarity (SSIM). SSIM is conventionally used for evaluation of the multiregional segmentation accuracy. This parameter evaluates degradation and change of the structural information. The structural information represent idea that pixels have strong inter-dependencies, especially when they are spatially close. Based on the experimental testing, the structural information is also depended on the image resolution (Table 24). Decreasing number of pixels degrades SSIM parameter. Among alternative tested methods, the proposed method achieves the highest SSIM results. Higher values of the SSIM indicates better results.

Lastly, we evaluate the FSIM parameter (Table 25). FSIM evaluates a local image quality. As well as in the previous cases, higher FSIM corresponds with better result. As well as this parameter is depended on the image resolution. Also, this parameter achieves the best results for the proposed segmentation model.

Table 23. Quantitative comparison for modified ABC, ABC, GA and Particle Swarm Optimization (PSO) based on the Peak Signal-to-Noise Ratio (PSNR) [dB].

Testing IR Image [px]	n	PSNR [dB]			
		Modified ABC	ABC	GA	PSO
640 × 480	1	27.11	26.54	26.99	29.98
	2	27.03	26.45	26.98	26.92
	3	26.78	25.92	26.74	27.78
	4	26.77	26.54	25.84	26.71
	5	27.13	27.11	26.87	26.98
500 × 500	1	25.12	25.01	24.33	24.98
	2	26.12	25.87	25.44	25.51
	3	25.45	25.32	25.87	24.65
	4	26.17	25.93	25.45	26.01
	5	24.65	24.87	25.11	24.84
300 × 300	1	24.45	23.44	23.87	24.15
	2	23.98	23.65	24.11	24.05
	3	24.54	24.21	23.59	23.93
	4	23.84	23.45	23.11	23.81
	5	22.84	23.13	24.54	23.41
50 × 50	1	21.45	21.21	21.35	20.48
	2	21.65	21.36	20.48	20.16
	3	20.84	20.65	20.94	21.13
	4	21.32	20.45	20.84	20.44
	5	21.55	20.98	20.74	21.43

Table 24. Quantitative comparison for modified ABC, ABC, GA, and PSO based on the SSIM.

Testing IR Image [px]	n	SSIM			
		Modified ABC	ABC	GA	PSO
640 × 480	1	0.94	0.87	0.72	0.91
	2	0.98	0.91	0.94	0.79
	3	0.89	0.91	0.78	0.88
	4	0.93	0.91	0.87	0.88
	5	0.96	0.89	0.73	0.79
500 × 500	1	0.77	0.81	0.74	0.75
	2	0.90	0.73	0.79	0.89
	3	0.59	0.93	0.69	0.78
	4	0.79	0.71	0.73	0.74
	5	0.82	0.83	0.76	0.77
300 × 300	1	0.65	0.67	0.45	0.59
	2	0.64	0.61	0.52	0.59
	3	0.74	0.71	0.68	0.69
	4	0.82	0.81	0.74	0.58
	5	0.79	0.81	0.78	0.80
50 × 50	1	0.66	0.61	0.62	0.65
	2	0.69	0.45	0.49	0.53
	3	0.74	0.75	0.73	0.65
	4	0.78	0.65	0.67	0.69
	5	0.74	0.76	0.74	0.81

Table 25. Quantitative comparison for modified ABC, ABC, GA, and PSO based on the FSIM.

Testing IR Image [px]	n	FSIM			
		Modified ABC	ABC	GA	PSO
640 × 480	1	0.88	0.84	0.87	0.83
	2	0.95	0.77	0.81	0.93
	3	0.91	0.88	0.89	0.93
	4	0.79	0.77	0.68	0.78
	5	0.87	0.86	0.86	0.84
500 × 500	1	0.69	0.72	0.73	0.75
	2	0.72	0.71	0.65	0.71
	3	0.83	0.81	0.79	0.68
	4	0.81	0.74	0.79	0.80
	5	0.78	0.81	0.78	0.81
300 × 300	1	0.65	0.69	0.64	0.64
	2	0.72	0.71	0.59	0.63
	3	0.65	0.69	0.61	0.59
	4	0.78	0.71	0.73	0.74
	5	0.77	0.73	0.74	0.68
50 × 50	1	0.59	0.57	0.45	0.53
	2	0.54	0.51	0.52	0.61
	3	0.61	0.54	0.59	0.60
	4	0.68	0.55	0.58	0.59
	5	0.71	0.68	0.56	0.70

7. Discussion and Future Perspectives

Alcohol intoxication is frequently discussed area due to its large importance. There are conventional methods, which can detect and measure the alcohol content, for example, breath or blood analysis. On the other hand, such methods usually serve for on-spot measurement, do not allow dynamical tracking of alcohol intoxication, and require awareness of the tested person. Safety systems would need additive systems allowing for automatic indication and classification of people, who may be under the alcohol influence.

Despite conventional methods, alcohol may be estimated based on facial features representing a dynamical progress of facial temperature distribution. The current reviewed papers show that alcohol intoxication may be estimated via extraction of the facial features, which are linked with real intoxication. One of the limitations of the current literature is its binary recognition: sober/drunken. Such an approach does not allow tracking of the dynamical features as markers of alcohol intoxication. In our analysis, we use the idea that the IR facial image domain can be decomposed via the multiregional segmentation to identify and classify the temperature-facial features being changed within the gradual intoxication.

One of the crucial parts of IR facial image analysis is the dataset. We have done two measurement with twenty tested persons. Our results show that multiregional segmentation is capable of identifying the facial areas in the nose and forehead, which show significant temperature variations whilst alcohol drinking. The relevance of the results is also supported by correlating the analysis with breath analysis. This analysis shows a strong linear dependency between facial temperature and the breath analysis. On the other hand, we are aware of limitations of the analysis. We used one IR camera, and images were taken with unified resolution. It will be worth using different types of the IR cameras to compare the proposed model effectivity for different data sources.

In this paper, we bring a novel clustering scheme focused on the dynamical tracking of alcohol intoxication from IR images. Unlike conventional methods intended for on-spot measurement of a level of intoxication, we analyzed thermal facial features enabling dynamical tracking of gradual intoxication.

A multiregional segmentation allows for a decomposition of the facial IR image into finite intensity bands. Segmentation based on the clustering performs this decomposition based on the intensity

features similarity. This similarity can be measured via distance function, which classifies respective facial temperature to such a cluster with a minimal distance. One of the major limitations of the K-means clustering is the initial centroids placement. For this task, there is no scheme versatility applicable for any image data. The proposed method, which utilizes evolutionary optimization on the modified ABC algorithm, generates a finite number of possible solutions of the centroids' placement which are evaluated during the optimization process. For this task, statistical variance is used to evaluate the quality of the respective solution within the evolutionary optimization.

The proposed multiregional segmentation model identifies a finite number of clusters containing thermal facial intensities with closely similar features. Based on the experimental results, we have performed modeling of the hottest facial temperature spectrum in the forehead, and the coldest spectrum in the nose. These model's features show the dynamical trend of facial temperature distribution whilst alcohol drinking. Lastly, we have objectivized the proposed segmentation model based on selected parameters. Judging by the experimental results, the proposed method appear to be the most robust, when comparing with selected alternative methods, even in the noisy environment.

The proposed model is primarily intended for the modeling and extraction of the facial-temperature areas which express significant dynamical development whilst gradual alcohol drinking. The further challenging issue may be classification of the respective stages of intoxication. Also, there are other aspects, which should be significant regarding modeling intoxication. Various people may have different inclinations to alcohol consumption or to types of particular alcohol. These aspects may be noticeable in the IR facial records. Thus, the sensitivity of the model of such phenomena is important for further development in this area. Lastly, the residual alcohol modeling may be important in this model. In the future it will be worth investigating the model robustness and sensitivity in the stated features.

Author Contributions: Conceptualization, B.F.-B; formal analysis, M.P., C.N., T.K. and M.A.; funding acquisition, M.P. and M.C.; investigation, J.K. and A.K.; methodology, J.K. and D.V.; project administration, M.C. and J.K.; resources, M.P. and M.A.; software, M.P. and E.K.; supervision, J.K. and D.V.; validation, D.V., R.S. and J.K.; visualization, M.A.; writing—original draft, J.K. and D.V.; writing—review and editing, J.K., M.C., D.V. and M.P.

Funding: This research received no external funding.

Acknowledgments: The work and the contributions were supported by the project SV4508811/2101Biomedical Engineering Systems XIV'. This study was also supported by the research project The Czech Science Foundation (GACR) 2017 No. 17-03037S Investment evaluation of medical device development run at the Faculty of Informatics and Management, University of Hradec Kralove, Czech Republic. This study was supported by the research project The Czech Science Foundation (TACR) ETA No. TL01000302 Medical Devices development as an effective investment for public and private entities.

Conflicts of Interest: The authors of the paper declare that do not have any conflict of interest.

References

1. Jadhav, K.S.; Magistretti, P.J.; Halfon, O.; Augsburger, M.; Boutrel, B. A preclinical model for identifying rats at risk of alcohol use disorder. *Sci. Rep.* **2017**, *7*, 9454. [[CrossRef](#)] [[PubMed](#)]
2. Ghorbani, H.; Nezami, A.; Sheikholeslami, B.; Hedjazi, A.; Ahmadimanesh, M. Simultaneous measurement of formic acid, methanol and ethanol in vitreous and blood samples of postmortem by headspace GC-FID. *J. Occup. Med. Toxicol.* **2018**, *13*, 1. [[CrossRef](#)] [[PubMed](#)]
3. Harvey, A.J.; Bayless, S.J.; Hyams, G. Alcohol increases inattentive blindness when cognitive resources are not consumed by ongoing task demands. *Psychopharmacology* **2018**, *235*, 309–315. [[CrossRef](#)] [[PubMed](#)]
4. Korucuoglu, O.; Sher, K.J.; Wood, P.K.; Sauls, J.S.; Altamirano, L.; Miyake, A.; Bartholow, B.D. Acute alcohol effects on set-shifting and its moderation by baseline individual differences: A latent variable analysis. *Addiction* **2017**, *112*, 442–453. [[CrossRef](#)] [[PubMed](#)]
5. Ljungblad, J.; Hök, B.; Ekström, M. Development and Evaluation of Algorithms for Breath Alcohol Screening. *Sensors* **2016**, *16*, 469. [[CrossRef](#)] [[PubMed](#)]
6. McCrae, J.C.; Sharkey, N.; Webb, D.J.; Vliegthart, A.D.B.; Dear, J.W. Ethanol consumption produces a small increase in circulating MIR-122 in healthy individuals. *Clin. Toxicol.* **2016**, *54*, 53–55. [[CrossRef](#)]

7. Andrade, J.D.S.; Rocha, C.E.; Maciel, M.A.V.; Santana, D.C.A.S.; Santana, F.J.M. Prevalence and risk of potentially adverse drug interactions in the treatment of acute alcohol poisoning. *Braz. J. Pharm. Sci.* **2016**, *52*, 133–141. [\[CrossRef\]](#)
8. Hartung, B.; Schwender, H.; Pawlik, E.; Ritz-Timme, S.; Mindiashvili, N.; Daldrup, T.; Information, P.E.K.F.C. Comparison of venous blood alcohol concentrations and breath alcohol concentrations measured with Draeger Alcotest 9510 DE Evidential. *Forensic Sci. Int.* **2016**, *258*, 64–67. [\[CrossRef\]](#)
9. Gjerde, H.; Romeo, G.; Mørland, J. Challenges and common weaknesses in case-control studies on drug use and road traffic injury based on drug testing of biological samples. *Ann. Epidemiol.* **2018**, *28*, 812–820. [\[CrossRef\]](#)
10. Bullock, M.; Ranse, J.; Hutton, A. Impact of Patients Presenting with Alcohol and/or Drug Intoxication on In-Event Health Care Services at Mass-Gathering Events: An Integrative Literature Review. *Prehosp. Disaster Med.* **2018**, *33*, 539–542. [\[CrossRef\]](#)
11. Martinek, R.; Razera, G.; Kahankova, R.; Židek, J. Optimization of the training symbols for minimum mean square error equalizer. *Adv. Intell. Syst. Comput.* **2018**, *565*, 272–287.
12. Ray, L.A.; Bujarski, S.; Roche, D.J.O. Subjective Response to Alcohol as a Research Domain Criterion. *Alcohol. Clin. Exp. Res.* **2016**, *40*, 6–17. [\[CrossRef\]](#)
13. Zhihua, X.; Peng, J.; Ying, X.; Ke, L. Drunk identification using far infrared imagery based on DCT features in DWT domain. In Proceedings of the International Symposium on Optoelectronic Technology and Application, Beijing, China, 25 October 2016. [\[CrossRef\]](#)
14. Koukiou, G.; Anastassopoulos, V. Neural networks for identifying drunk persons using thermal infrared imagery. *Forensic Sci. Int.* **2015**, *252*, 69–76. [\[CrossRef\]](#)
15. Hiass, R.S.; Arandjelović, O.; Bendada, H.; Maldague, X. Vesselness features and the inverse compositional AAM for robust face recognition sing thermal IR. In Proceedings of the 27th AAAI Conference on Artificial Intelligence, Bellevue, WA, USA, 14–18 July 2013; pp. 357–364.
16. Bhuyan, M.K.; Dhawle, S.; Sasmal, P.; Koukiou, G. Intoxicated Person Identification Using Thermal Infrared Images and Gait. In Proceedings of the 2018 International Conference on Wireless Communications, Signal Processing and Networking (WiSPNET), Chennai, India, 22–24 March 2018.
17. Koukiou, G.; Anastassopoulos, V. Drunk person identification using thermal infrared images. *Int. J. Electron. Secur. Digit. Forensics* **2012**, *4*, 229–243. [\[CrossRef\]](#)
18. Koukiou, G.; Anastassopoulos, V. Facial blood vessels activity in drunk persons using thermal infrared. In Proceedings of the 4th International Conference on Imaging for Crime Detection and Prevention 2011 (ICDP 2011), London, UK, 3–4 November 2011; pp. 1–4.
19. Koukiou, G.; Anastassopoulos, V. Drunk person screening using eye thermal signatures. *J. Forensic Sci.* **2016**, *61*, 259–264. [\[CrossRef\]](#)
20. Fernández-Cuevas, I.; Bouzas Marins, J.C.; Arnáiz Lastras, J.; Gómez Carmona, P.M.; Piñonosa Cano, S.; García-Concepción, M.Á.; Sillero-Quintana, M. Classification of factors influencing the use of infrared thermography in humans: A review. *Infrared Phys. Technol.* **2015**, *71*, 28–55. [\[CrossRef\]](#)
21. Tan, J.-H.; Ng, E.; Acharya, U.R.; Chee, C. Infrared thermography on ocular surface temperature: A review. *Infrared Phys. Technol.* **2009**, *52*, 97–108. [\[CrossRef\]](#)
22. Ammer, K.; Ring, E.F. Influence of the field of view on temperature readings from thermal images. *Thermol. Int.* **2005**, *15*, 99–103.
23. Koukiou, G.; Anastassopoulos, V. Drunk person identification using local difference patterns. In Proceedings of the 2016 IEEE International Conference on Imaging Systems and Techniques (IST), Chania, Greece, 4–6 October 2016; pp. 401–405.
24. Socolinsky, D.A.; Selinger, A. Thermal face recognition over time Proceedings. In Proceedings of the 17th International Conference on Pattern Recognition, Cambridge, UK, 26 August 2004; Volume 4, pp. 187–190.
25. Socolinsky, D.A.; Selinger, A. A comparative analysis of face recognition performance with visible and thermal infrared imagery. In Proceedings of the Object Recognition Supported by User Interaction for Service Robots, Quebec City, QC, USA, 11–15 August 2002; Volume 16, pp. 217–222.
26. Shirizadeh, A.; Haghipour, S.; Sakhavati, A. Physiology-based face recognition in the thermal infrared spectrum. *Life Sci. J.* **2013**, *10*, 540–545.

27. Khan, M.M.; Ingleby, M.; Ward, R.D. Automated Facial Expression Classification and affect interpretation using infrared measurement of facial skin temperature variations. *ACM Trans. Auton. Adapt. Syst.* **2006**, *1*, 91–113. [\[CrossRef\]](#)
28. Zhao, S.; Grigat, R.-R. An Automatic Face Recognition System in the Near Infrared Spectrum. *Comput. Vis. ECCV* **2005**, 3587, 437–444.
29. Hermosilla, G.; Verdugo, J.L.; Farias, G.; Vera, E.; Pizarro, F.; Machuca, M. Face Recognition and Drunk Classification Using Infrared Face Images. *J. Sens.* **2018**, 2018. [\[CrossRef\]](#)
30. Hubicka, B.; Bergman, H.; Laurell, H. Psychosocial characteristics of drunk drivers assessed by the Addiction Severity Index, prediction of relapse. *Scand. J. Public Health* **2010**, *38*, 71–77. [\[CrossRef\]](#)
31. Khan, M.M.; Ward, R.D.; Ingleby, M. Classifying pretended and evoked facial expressions of positive and negative affective states using infrared measurement of skin temperature. *ACM Trans. Appl. Percept.* **2009**, *6*, 1–22. [\[CrossRef\]](#)
32. Wang, Y.; Teng, Z.; Wen, H.; Li, J.; Martinek, R. A state evaluation adaptive differential evolution algorithm for fir filter design. *Adv. Electr. Electron. Eng.* **2017**, *15*, 770–779. [\[CrossRef\]](#)
33. García, I.; Bronte, S.; Bergasa, L.M.; Hernandez, N.; Delgado, B.; Sevillano, M. Vision-based drowsiness detector for a realistic driving simulator. In Proceedings of the 13th International IEEE Conference on Intelligent Transportation Systems, Funchal, Portugal, 19–22 September 2010; pp. 887–894.
34. Voisan, E.-I.; Marginean, O.; Precup, R.-E.; Dragan, F.; Purcaru, C. Performance evaluation of a face detection algorithm running on general purpose operating systems. In Proceedings of the 2013 IEEE 8th International Symposium on Applied Computational Intelligence and Informatics (SACI), Timisoara, Romania, 23–25 May 2013; pp. 163–168.
35. Sanli, O.; Ilgen, B. Face detection and recognition for automatic attendance system. *Adv. Intell. Syst. Comput.* **2019**, *868*, 237–245.
36. Ma, H.; Shen, S.; Yu, M.; Yang, Z.; Fei, M.; Zhou, H. Multi-population techniques in nature inspired optimization algorithms: A comprehensive survey. *Swarm Evolut. Comput.* **2019**, *44*, 365–387. [\[CrossRef\]](#)
37. Jino Ramson, S.R.; Lova Raju, K.; Vishnu, S.; Anagnostopoulos, T. Nature inspired optimization techniques for image processing—A short review. *Intell. Syst. Ref. Libr.* **2019**, *150*, 113–145.
38. Hassanien, A.E.; Abraham, A.; Peters, J.F.; Schaefer, G.; Henry, C. Rough sets and near sets in medical imaging: A review. *IEEE Trans. Inf. Technol. Biomed.* **2009**, *13*, 955–968. [\[CrossRef\]](#)
39. Karaboga, D. *An Idea Based on Honey Bee Swarm for Numerical Optimization*; Erciyes University: Kayseri, Turkey, 2005.
40. Kiran, M.S.; Findik, O. A directed artificial bee colony algorithm. *Appl. Soft Comput. J.* **2015**, *26*, 454–462. [\[CrossRef\]](#)
41. Bhandari, A.; Kumar, A.; Singh, G. Modified artificial bee colony based computationally efficient multilevel thresholding for satellite image segmentation using Kapur's, Otsu and Tsallis functions. *Expert Syst. Appl.* **2015**, *42*, 1573–1601. [\[CrossRef\]](#)
42. Zhao, W.; Lv, Y.; Liu, Q.; Qin, B. Detail-Preserving Image Denoising via Adaptive Clustering and Progressive PCA Thresholding. *IEEE Access* **2018**, *6*, 6303–6315. [\[CrossRef\]](#)
43. Jang, J.; Bang, K.; Jang, H.; Hwang, D.; The Alzheimer's Disease Neuroimaging Initiative. Quality evaluation of no-reference MR images using multidirectional filters and image statistics. *Magn. Reson. Med.* **2018**, *80*, 914–924. [\[CrossRef\]](#)
44. Zhang, J.; Wang, X.; Yang, C.; Zhang, J.; He, D.; Song, H. Image dehazing based on dark channel prior and brightness enhancement for agricultural remote sensing images from consumer-grade cameras. *Comput. Electron. Agric.* **2018**, *151*, 196–206. [\[CrossRef\]](#)
45. Shahdoosti, H.R.; Mehrabi, A. Multimodal image fusion using sparse representation classification in tetrolet domain. *Digit. Sign. Process.* **2018**, *79*, 9–22. [\[CrossRef\]](#)
46. Kang, X.-B.; Zhao, F.; Lin, G.-F.; Chen, Y.-J. A novel hybrid of DCT and SVD in DWT domain for robust and invisible blind image watermarking with optimal embedding strength. *Multimed. Tools Appl.* **2018**, *77*, 13197–13224. [\[CrossRef\]](#)
47. Dai, T.; Gu, K.; Niu, L.; Zhang, Y.-B.; Lu, W.; Xia, S.-T. Referenceless quality metric of multiply-distorted images based on structural degradation. *Neurocomputing* **2018**, *290*, 185–195. [\[CrossRef\]](#)

48. Kim, K.; Kim, W.; Kang, S.; Park, C.; Lee, D.; Cho, H.; Seo, C.; Lim, H.; Lee, H.; Kim, G.; et al. A blind-deblurring method based on a compressed-sensing scheme in digital breast tomosynthesis. *Opt. Lasers Eng.* **2018**, *110*, 228–235. [[CrossRef](#)]
49. Mittal, H.; Saraswat, M. An optimum multi-level image thresholding segmentation using non-local means 2D histogram and exponential Kbest gravitational search algorithm. *Eng. Appl. Artif. Intell.* **2018**, *71*, 226–235. [[CrossRef](#)]
50. Fang, Y.; Yan, J.; Li, L.; Wu, J.; Lin, W. No Reference Quality Assessment for Screen Content Images with Both Local and Global Feature Representation. *IEEE Trans. Image Process.* **2018**, *27*, 1600–1610. [[CrossRef](#)]
51. Das, K.; Maitra, M.; Sharma, P.; Banerjee, M. Early started hybrid denoising technique for medical images. *Adv. Intell. Syst. Comput.* **2019**, *727*, 131–140.
52. Savvas, I.K.; Garani, G. Perspectives of fast clustering techniques. *Adv. Intell. Syst. Comput.* **2019**, *875*, 31–40.
53. Garani, G.; Adam, G.K.; Ventzas, D. Temporal data warehouse logical modelling. *Int. J. Data Min. Model. Manag.* **2016**, *8*, 144. [[CrossRef](#)]



© 2019 by the authors. Licensee MDPI, Basel, Switzerland. This article is an open access article distributed under the terms and conditions of the Creative Commons Attribution (CC BY) license (<http://creativecommons.org/licenses/by/4.0/>).